SIAM J. Applied Dynamical Systems
Vol. 12, No. 1, pp. 279–314

Contrasting Existence and Robustness of REM/Non-REM Cycling in Physiologically Based Models of REM Sleep Regulatory Networks*

Cecilia G. Diniz Behn†, Aparna Ananthasubramaniam‡, and Victoria Booth§

Abstract. Typical human sleep throughout the night consists of alternating periods of rapid eye movement (REM) sleep and non-REM (NREM) sleep. This ultradian rhythm of NREM/REM cycling is thought to be produced by the state-dependent activity of "REM-on" and "REM-off" brainstem and hypothalamic neuronal populations that, respectively, promote or suppress REM sleep. Synaptic interactions among these populations define REM sleep regulatory networks; however, the identity of the key neuronal populations in these networks and the dynamics of interactions among them are disputed and cannot be addressed comprehensively with current experimental techniques. The purpose of this study is to use physiologically based mathematical models to explore the dynamic implications associated with competing hypotheses for network-based REM sleep regulation. Generally, putative REM sleep regulatory networks fall into two categories: a reciprocal interaction network consisting of an excitatory REM-on population interacting with an inhibitory REM-off population, and a mutual inhibition network where both REM-on and REM-off populations are inhibitory. We focus on the generation of regular periodic cycling solutions, which would generate the NREM/REM ultradian rhythm, in these networks. By applying our understanding of network mechanisms, we develop efficient numerical criteria for the existence of stable cycling solutions in each network structure. To investigate the robustness of cycling, we systematically analyze the response of model dynamics to manipulation of the components governing network interactions. By establishing the implications of network structure for the mechanisms and dynamics of NREM/REM state transitions, this comparative analysis identifies key targets for future experimental work to distinguish the structure of the proposed physiological REM sleep regulatory network.

Key words. firing rate model, oscillations, bifurcation analysis, limit cycle, hysteresis, bistability, sensitivity analysis

AMS subject classifications. 34C23, 34C25, 34C55, 37G10, 37N25, 70K70, 92C20

DOI. 10.1137/120876939

1. Introduction.

Physiologically based mathematical modeling of sleep-wake behavior offers a novel technique for probing the putative neural mechanisms generating transitions between wake and sleep states. Human sleep is composed of both rapid eye movement (REM) sleep and non-REM (NREM) sleep, and the transitions among states of wake, NREM sleep, and REM sleep have distinct, stereotyped properties. The structure of a typical consolidated nighttime sleep period begins with NREM sleep and reveals a robust cyclic alternation between NREM and REM sleep over the course of the night. Known as the ultradian rhythm, these

*Received by the editors May 14, 2012; accepted for publication (in revised form) by E. Sander November 4, 2012; published electronically February 14, 2013. This work was partially supported by the Air Force Office of Scientific Research grant FA9550-08-1-0111 and National Science Foundation grant DMS 1121361.
http://www.siam.org/journals/siads/12-1/87693.html
†Department of Mathematics, University of Michigan, Ann Arbor, MI, and Department of Mathematics, Gettysburg College, Gettysburg, PA (cdinizbe@gettysburg.edu).
‡Department of Mathematics, Stanford University, Stanford, CA (akananth@stanford.edu).
§Departments of Mathematics and Anesthesiology, University of Michigan, Ann Arbor, MI (vbooth@umich.edu).

cycles are approximately 90–110 minutes in adults [6]. This cyclic alternation provides a key constraint for models attempting to simulate human sleep-wake behavior.

The production of and transitions among states of wake, NREM sleep, and REM sleep are thought to be governed by neuronal populations in the brainstem and hypothalamus (reviewed in [40, 41]), though the specific populations involved in the regulation of REM sleep and their synaptic interactions are much debated [32, 4, 42, 8, 26]. Experiments investigating sleep-wake physiology are typically conducted in animals, but much of the anatomy and physiology of the sleep-wake regulatory network appears to be conserved across mammalian species [34]. Hence, we expect a network for REM sleep regulation, though characterized in rodents, to be capable of producing the robust ultradian cycling observed in human sleep.

The classical hypothesis for REM sleep regulation proposes that excitatory REM-promoting (REM-on) neuronal populations interact with inhibitory REM-suppressing (REM-off) neuronal populations to produce REM-on/REM-off cycling during sleep [32, 30]. However, recent experimental evidence has challenged the neurophysiological basis for this reciprocal interaction model, and several competing conceptual models for REM sleep regulation have been proposed [4, 42, 8, 26, 29]. Although there are differences in the REM-on and REM-off neuronal populations specified by distinct conceptual models, these models share an underlying structure of mutually inhibitory projections between REM-on and REM-off populations. Hence, the reciprocal interaction (RI) and mutual inhibition (MI) network structures represent two competing hypotheses for network-based REM sleep regulation.

Experimental investigation of the dynamic interactions among identified REM-on and REM-off populations is limited by the fact that REM sleep exists only in the intact animal. No reduced experimental preparation, such as brain slice or in situ preparation, which could permit close study of the time-varying activity of the interactions between neuronal populations, has been identified to exhibit any characteristics of sleep or waking states. As a result, the experimental techniques available to probe the putative REM sleep regulatory network are limited to those that can be conducted in vivo without disrupting sleep, or postmortem studies that can identify anatomy but not dynamic interactions.

Therefore, although conceptual network models are formulated to be consistent with identified activity of various neuronal populations during each sleep-wake state, the implications of the structure of these networks for the mechanisms and dynamics of state transitions are not well understood. In previous work, we focused on investigating the mechanisms associated with the state transitions among wake, NREM sleep, and REM sleep with an emphasis on relating results to known physiology and providing insights into the fine architecture of sleep-wake behavior [17, 14, 20, 15, 16]. The purpose of this study is to explicitly explore the dynamic implications associated with the two competing hypotheses for network-based REM sleep regulation. Using a general modeling framework, we develop minimal mathematical models of abstract RI and MI networks. We identify conditions for the generation of regular periodic cycling in each putative REM regulatory network and establish distinctions between the networks by examining changes in cycling dynamics in response to manipulations of network components.

Specifically, in this study, we analyze the existence and robustness of stable periodic cycling solutions in minimal mathematical models of the RI and MI REM sleep regulatory networks. In each model, periodic cycling is generated by a different dynamic mechanism: by

limit cycle oscillations in the RI network and by hysteresis-loop cycling in the MI network. By applying our understanding of network mechanisms, we develop efficient numerical criteria for the existence of stable cycling solutions in each network. To investigate the robustness of cycling, we systematically analyze the response of model dynamics to manipulation of the components governing network interaction, namely, the reciprocal synaptic projections between the REM-on and REM-off populations and self-modulatory inputs that account for intrinsic excitability properties of each population. Since these interaction and self-modulatory parameters are present in both models, this analysis identifies differences between model responses to manipulation of the same network component, thus making predictions of changes to REM sleep patterning under these manipulations. Since REM sleep patterning is the primary experimentally accessible marker of activity of the REM sleep regulatory network, our results provide insight into targets for further experimental investigation that may distinguish the structure of the proposed physiological REM sleep regulatory network.

The remainder of this paper is organized as follows. Section 2 introduces the mathematical modeling formalism used to describe the REM sleep regulatory networks. Sections 3 and 4 present existence and robustness results for cycling in the RI and MI models, respectively. Section 5 compares cycling sensitivity in the different models for REM sleep regulation. Section 6 summarizes our results and discusses the broader physiological implications of our analyses.

2. Methods and models.

2.1. Network structures for REM sleep regulatory networks. Many neuronal populations in the brainstem and hypothalamus are thought to participate in the regulation of REM sleep [32, 4, 42, 8, 26]. Although multiple populations may be involved, the underlying mechanisms in conceptual models for network-based REM sleep regulation can be broadly classified as RI or MI. We will focus on these underlying network structures rather than on modeling specific neuronal populations. As described in the introduction, an RI structure involves excitation from a REM-on (R) population to a REM-off/NREM-on (N) population and inhibition from the N to the R population; by contrast, the MI structure assumes bidirectional inhibition between R and N. As discussed below, the MI network requires an external drive in order to produce a regular oscillation, and we will argue that this drive represents a REM-sleep-specific homeostatic drive. Since the physiological basis for the REM sleep homeostatic drive is not well understood, we consider two cases for the MI network: one in which the external drive acts on the N population (MIHN), and one in which it acts on the R population (MIHR) (Figure 1).

2.2. Reduced population modeling formalism. To model the neurotransmitter-mediated interaction between neuronal populations, we use a reduced version of a previously developed population firing rate model formalism [14, 16]. In this section we describe the general form of model equations and identify the parameters associated with each model. Since we model generalized neuronal populations, most parameters, with the exception of those governing coupling and auto-effects, are the same for all models. In previous work, we determined ranges for these parameters; ranges were based on experimental data whenever possible [14, 16]. Unless otherwise noted, the parameter values used here are consistent with these ranges. For example, in a 3-population model with wake-, NREM sleep-, and REM sleep-promoting

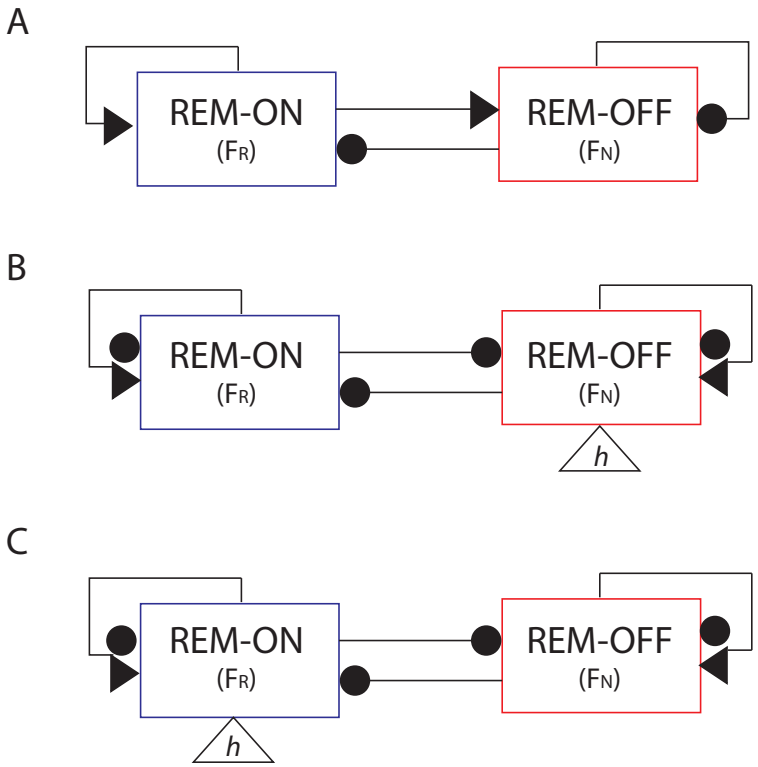

Figure 1. *Schematics for proposed REM sleep regulatory networks. For synaptic coupling between neuronal populations, circles denote inhibition, and arrows denote excitation.* A. *The RI network has established cross- and auto-effects: The REM-on population (F_R, blue) is excitatory, and the REM-off population (F_N, red) is inhibitory.* B, C. *The MI network requires external input to oscillate, so we separately consider cases in which this input, in the form of a REM sleep homeostatic drive, h, acts on the REM-off (MIHN,* B*) and REM-on (MIHR,* C*) populations, respectively. Since, for different populations, auto-effects may be inhibitory or excitatory, we allow both possibilities in the model structure.*

populations, the maximal firing rates for each population were $W_{max} = 6.5$ Hz, $N_{max} = 5$ Hz, and $R_{max} = 5$ Hz, respectively, based on experimental data associated with the neuronal populations represented by our model populations [16]. For the general models presented here, the maximal firing rates were chosen to be 5 Hz for all populations.

In the original modeling formalism, the firing rate of a presynaptic population, $F_X(t)$, induces expression of neurotransmitter concentration, $C_X(t)$, which drives the postsynaptic firing rate [14]. In the reduced model formalism used here, neurotransmitter dynamics are assumed to be deterministic and instantaneous: $C_X(t)$ is replaced with the value predicted by its steady-state release function $C_{X\infty}(F_X)$ [16]. The implied assumption that the dynamics of $C_X(t)$ are much faster than those of $F_X(t)$ is a reduction in the dimension of the model and is not meant to represent physiological characteristics of the system. Analysis of the original model formalism has indicated that inclusion of time-varying $C_X(t)$ can affect fine time scale and highly variable dynamics of model solutions that come into play when modeling the fast state transitions in rodent sleep [14]. In a deterministic model and for the longer time scale dynamics associated with human ultradian cycling, the model reduction does not qualitatively

affect solution dynamics, particularly the appearance of stable equilibrium solutions that disrupt cycling, which we focus on in this study.

The equations for the firing rates of the REM-on (F_R) and REM-off (F_N) populations in the RI, MIHN, and MIHR models are given by

$$\begin{aligned} F_R' &= \frac{F_{R\infty}[g_{N,R}C_{N\infty}(F_N) + g_{R,R}C_{R\infty}(F_R)] - F_R}{\tau_R}, \\ F_N' &= \frac{F_{N\infty}[g_{R,N}C_{R\infty}(F_R) + g_{N,N}C_{N\infty}(F_N)] - F_N}{\tau_N}, \end{aligned} \tag{2.1}$$

where $F_{R\infty}(\cdot)$ and $F_{N\infty}(\cdot)$ are the steady-state firing rate response functions for the REM-on and REM-off populations, respectively. The arguments of these functions contain the sum of neurotransmitter concentrations $C_{X\infty}$ acting on the population. The neurotransmitter steady-state release functions have the following form:

$$C_{X\infty}(F_X) = \tanh(F_X/\gamma_X) \quad (X = R, N), \tag{2.2}$$

where the parameter γ_X controls the sensitivity of release as a function of presynaptic firing rate F_X and is set to the value $\gamma_R = \gamma_N = 5$ in all models. Based on existing physiological data, we would expect C_R to represent acetylcholine and C_N to represent noradrenaline in the RI model, and we would expect both C_R and C_N to represent GABA in the MI models [32, 4, 42, 8, 26]. However, no neurotransmitter-specific assumptions have been incorporated into $C_{R\infty}$ or $C_{N\infty}$. Steady-state neurotransmitter concentration $C_{X\infty}(\cdot)$ is normalized between 0 and 1 due to the variability of experimental measurements of absolute neurotransmitter concentrations, and the effect on postsynaptic population Y is weighted by the constant parameter $g_{X,Y}$, where the sign of each $g_{X,Y}$ distinguishes between an excitatory ($g_{X,Y} > 0$) or an inhibitory ($g_{X,Y} < 0$) effect of the neurotransmitter. The self-coupling or auto-effect terms $g_{R,R}$ and $g_{N,N}$ account for intrinsic excitability properties of the populations.

The firing rates $F_X(t)$ (in Hz, $X = R, N$) evolve to steady-state values with time constants τ_X which are set to $\tau_R = \tau_N = 1$ min in all models. This value is larger than that used in previous work and may reflect the longer transition times between REM and NREM sleep in humans compared to rodents [44]. The steady-state firing rate response functions $F_{X\infty}(\cdot)$ have the sigmoidal profile used in standard firing rate models [51] (see reviews in [19, 9, 11]):

$$F_{X\infty}(c) = X_{max}(0.5(1 + \tanh((c - \beta_X)/\alpha_X))). \tag{2.3}$$

Maximum firing rates are set to $R_{max} = N_{max} = 5$ Hz, and the sensitivities of response are set to $\alpha_R = \alpha_N = 0.5$ in all models. In the RI model, the half-activation thresholds of the firing rate response functions are constants and set to $\beta_R = 0$ and $\beta_N = 1.5$. In the MI models, these half-activation thresholds are set to -0.5 when they are not modulated by the REM sleep homeostatic drive (see below).

We interpret cycling in the model solutions to be the regular alternation between high and low levels of activity in the R and N populations; this defines the ultradian REM-NREM rhythm. In the RI model, the following default values of the neurotransmitter weighting parameters scaling the cross- and self-coupling effects of the populations produce stable periodic cycling solutions: $g_{R,R} = 6$; $g_{N,N} = -1$; $g_{N,R} = -7$; and $g_{R,N} = 7$. For the MIHN and MIHR

models, default cross- and self-coupling parameters are chosen to be $g_{R,R} = 0$; $g_{N,R} = -4$; $g_{R,N} = -1.5$; $g_{N,N} = 0$; and $g_{R,R} = 0$; $g_{N,N} = 0$; $g_{N,R} = -2$; and $g_{R,N} = -2$, respectively. In each model these default parameters produce robust periodic cycling solutions. Our analysis focuses on the existence of cycling solutions without specific constraints on the period of the oscillations. Results would not be qualitatively different in model parameter regimes with different cycle periods that remain in the range of human ultradian cycling in which state transition times are much shorter than cycle periods.

2.3. Modeling the REM sleep homeostatic drive. In contrast to the RI network, the MI networks, as modeled in our formalism, cannot cycle regularly without an external drive that periodically forces a transition between high activity in F_R and high activity in F_N. Although random transitions between high activity in F_R and F_N, interpreted as transitions between REM sleep and NREM sleep, could occur as a result of noise, a periodic external drive is necessary to produce regular ultradian oscillations. This requirement for an external drive reflects the inability of an isolated population to display oscillatory or excitable dynamics in this modeling formalism and contrasts with other types of mutually inhibitory neuronal network models, referred to as half-center oscillators [45, 49], that are capable of robust periodic cycling.

A physiological candidate for an external drive regulating transitions between the REM-on and REM-off populations is the concept of a homeostatic drive for REM sleep. Experiments involving total sleep deprivation and selective REM sleep deprivation have suggested that REM sleep is homeostatically regulated, i.e., that there exists a physiological need-based drive for REM sleep that increases in its absence and decreases in its presence (for a recent review see [1]). However, the mechanism and physiological basis of such a drive are not well understood, and there has been much debate about the qualitative features of a REM sleep homeostatic drive [21, 3].

The homeostatic drive for sleep, which increases with time awake to promote feelings of sleepiness and transitions into sleep, is slightly better understood. A leading candidate for one component of the physiological basis of the sleep homeostatic drive is adenosine, a somnogenic chemical whose levels increase during wakefulness and decrease during sleep [46, 7, 37, 43] and is thought to act in part by disinhibiting sleep-promoting neurons [7, 35, 22]. A number of sleep-wake regulatory network models include a homeostatic sleep drive that mimics adenosine dynamics by increasing toward a maximum value during wakefulness, decreasing toward 0 during sleep states, and modulating the response of the NREM sleep-promoting population to promote its activation as a function of time awake [14, 36, 38].

In the absence of a hypothesis for the physiological mechanisms underlying the homeostatic regulation of REM sleep, we use our previously developed formalism, based on the action of adenosine, in which a homeostatic drive variable modulates the half-activation threshold of the steady-state firing rate response function ($F_{X\infty}(\cdot)$; see (2.3)) [14]. However, since the state-dependencies and mechanisms of action of the REM sleep homeostatic drive are not constrained by a physiological correlate as they were for adensine, we consider multiple implementations of a REM sleep homeostatic drive. The state-dependent increase and decrease of the homeostatic drive variable may be gated by the N or R populations to result in REM-promoting or REM-terminating drives, respectively. Furthermore, the REM sleep

homeostatic drive may modulate the responses of either the N or R populations. In each of these implementations, the homeostatic dynamics are determined by the behavior of the R population; basing homeostatic dynamics on the behavior of the N population would yield analogous results, but it is less consistent with observed features of REM sleep homeostasis [50, 5, 18].

Under baseline network conditions, some of these implementations are equivalent. Therefore, we first establish equivalences among these different implementations of the REM sleep homeostatic drive.

2.3.1. Equivalences of the model REM sleep homeostatic drives. We model the action of the REM sleep homeostatic drive with the variable $h(t)$. The possible state-dependencies and sites of action of h yield the following four mechanisms for the REM sleep homeostatic drive:

1. *REM-terminating drive acting on the N-population.* h grows during REM sleep and decreases the half-activation threshold of $F_{N\infty}(\cdot)$, given by the parameter β_N, to promote activation of N and the transition to NREM sleep.
2. *REM-terminating drive acting on the R-population.* h grows during REM sleep and increases the half-activation threshold of $F_{R\infty}(\cdot)$, given by the parameter β_R, to promote inactivation of R and the transition to NREM sleep.
3. *REM-promoting drive acting on the N-population.* h grows during NREM sleep and increases the half-activation threshold of $F_{N\infty}(\cdot)$, given by the parameter β_N, to promote inactivation of N and the transition to REM sleep.
4. *REM-promoting drive acting on the R-population.* h grows during NREM sleep and decreases the half-activation threshold of $F_{R\infty}$, given by the parameter β_R, to promote activation of R and the transition to REM sleep.

Here we show that, under baseline network conditions, REM-promoting and REM-terminating state-dependencies produce equivalent long-term cycling behavior in an MI model, i.e., case 1 $\equiv$ case 3 and case 2 $\equiv$ case 4.

We will denote the REM-promoting REM sleep homeostatic drive by h_p and the REM-terminating REM sleep homeostatic drive by h_t. Consider h_p and h_t acting on the half-activation threshold of the N population, β_N; an equivalent argument exists for h_p and h_t acting on β_R. The variables h_p and h_t are governed by the following equations:

$$h_p' = \frac{(1-h_p)}{\tau_1} H[\theta_R - F_R] - \frac{h_p}{\tau_2} H[F_R - \theta_R], \tag{2.4}$$

$$h_t' = \frac{(1-h_t)}{\tau_2} H[F_R - \theta_R] - \frac{h_t}{\tau_1} H[\theta_R - F_R], \tag{2.5}$$

where $H[z]$ is the Heaviside function defined as $H[z] = 0$ if $z < 0$ and $H[z] = 1$ if $z \geq 0$. The state-dependence of homeostatic activity is gated by the firing rate of the REM-on population, F_R, relative to the threshold θ_R; if $F_R \geq \theta_R$, the network is in the REM state, and if $F_R < \theta_R$, the network is in the NREM state. The maximum value of h_p and h_t has been normalized to 1 without loss of generality; and τ_1 and τ_2 are the time constants associated with the change during NREM and REM sleep, respectively. Note that preserving the state association of τ_1 and τ_2 causes their associations with growth and decay to be interchanged.

Now applying the change of variables $h_p = 1 - h_t$, we see that the two equations governing h_p and h_t are equivalent. To conclude that the systems are equivalent, we impose constraints on initial conditions: the REM-promoting system with initial conditions F_{N0}, F_{R0}, and h_{p0} is equivalent to the REM-terminating system with initial conditions F_{N0}, F_{R0}, and $h_{t0} = 1 - h_{p0}$. Exploiting this equivalence between the systems under baseline network conditions, we will restrict further analysis of existence and robustness of cycling in the MI network to REM-terminating homeostatic drives. Results would be equivalent if a REM-promoting homeostatic drive were implemented. However, it is important to note that this equivalence applies to the isolated network only; in the presence of external inputs to the network, these equivalences may not hold. We also observe that distinct implementations have different implications for physiologic mechanisms and could exhibit different responses to any perturbation of the network (see the discussion in section 6).

2.3.2. Implementation of the REM sleep homeostatic drive. In our MI networks, we implement a REM-terminating REM sleep homeostatic drive acting on either the REM-off (MIHN) or REM-on (MIHR) population. The REM sleep homeostat is modeled by the variable $h(t)$ governed by the following equation:

$$h' = \frac{(1-h)}{\tau_2} H[F_R - \theta_R] - \frac{h}{\tau_1} H[\theta_R - F_R], \tag{2.6}$$

where $H[z]$ is the Heaviside function previously defined, and the F_R threshold for the REM state is set to $\theta_R = 1.5$ Hz. The time constants are set to $\tau_1 = \tau_2 = 30$ min. In the MIHN network, $h(t)$ modulates the half-activation threshold of $F_{N\infty}$, and (2.3) for $X = N$ is replaced by

$$F_{N\infty}(c) = N_{max}[0.5(1 + \tanh((c - \beta_N(h))/\alpha_N))], \quad \text{where} \quad \beta_N(h) = -2(h - 0.25). \tag{2.7}$$

The half-activation threshold for the R population is $\beta_R = -0.5$. In the MIHR network, $h(t)$ modulates the half-activation threshold of $F_{R\infty}$, and (2.3) for $X = R$ is replaced by

$$F_{R\infty}(c) = R_{max}[0.5(1 + \tanh((c - \beta_R(h))/\alpha_R))], \quad \text{where} \quad \beta_R(h) = 2(h - 0.75). \tag{2.8}$$

The half-activation threshold for the N population is $\beta_N = -0.5$.

2.4. Numerical approach to analyzing existence and robustness of cycling. For each model network, we establish conditions for cycling based on the existence and stability of fixed points, defined as solutions to (2.1) with $F_R' = F_N' = 0$, with the addition of (2.6) with $h' = 0$ for the MI models. To find fixed points numerically, we used the FindRoot function in *Mathematica* (Wolfram Research) which numerically solves a system of algebraic equations given an initial solution. We found all fixed points of each system by taking many initial points in the (F_N, F_R) plane specified by $[-1, 6] \times [-1, 6]$ for the RI model and from the (F_N, F_R, h) plane specified by $[-1, 6] \times [-1, 6] \times \{0, 1\}$ for the MI models.

To determine the stability of the fixed points, we computed the two-dimensional (2D) or three-dimensional (3D) Jacobian matrix and used the *Mathematica* Eigenvalue function to compute the eigenvalues of the matrix. In all cases, the existence of a stable fixed point was interpreted as sufficient to exclude robust ultradian cycling. In the RI case, the absence

of stable fixed points was necessary and sufficient to establish cycling. In the MI cases, the systems could fail to exhibit robust cycling even when no stable fixed points existed. This failure was linked to the role of the dynamics of the homeostat h and its interaction with the threshold θ_R; this case is discussed in more detail below.

To evaluate the robustness of cycling, we determined default parameter sets that produced ultradian cycling in each model. Then we varied pairs of coupling parameters to identify sensitivity of cycling to individual parameters and compensatory relationships among parameters. For each parameter pair, 2D bifurcation diagrams were constructed indicating the stable model solution in the parameter regime as determined by analysis of fixed points.

3. Reciprocal interaction model. In the RI model, the excitatory-inhibitory coupling between neuronal populations gives rise to robust cycling in the absence of external inputs. This is consistent with the cycling mechanism proposed by McCarley and colleagues in the original physiologically based models for REM sleep regulation by an RI network [32, 33]. In this section, we show that cycling in the general RI model occurs via a standard limit cycle mechanism, we derive numerical criteria for cycling to occur, and we analyze the robustness of this cycling to parameter variation.

3.1. Deriving numerical criteria for the existence of cycling in the RI model. Since the system is 2D, the existence of cycling in this model can be determined by numerical verification of criteria satisfying the Poincaré–Bendixson theorem [24]. We provide an outline of the approach.

First, we consider the (F_N, F_R) phase plane (Figure 2). The nullclines, $N_R = \{(F_N, F_R)|F'_R = 0\}$ and $N_N = \{(F_N, F_R)|F'_N = 0\}$, are continuous and defined for all real numbers. Using the intermediate value theorem, it is easy to show that the nullclines must intersect at least once. Each intersection point will be a fixed point of the system, and the stability of these fixed points will determine the long-term behavior of trajectories in the system.

We construct a rectangular trapping region with the following line segments: $\{F_N = -0.1\}$, $\{F_N = 5.1\}$, $\{F_R = -0.1\}$, and $\{F_R = 5.1\}$. From the relative orientation of the nullclines, it is clear that the vector field is inward-pointing along the boundary of this trapping region. To establish the existence of a stable limit cycle contained within the trapping region, it remains to show that there are no stable fixed points within the trapping region. To do this, we numerically identify all fixed points and evaluate their linear stability. We separately consider the cases of one or multiple fixed points. If there is only one fixed point in the trapping region, and it is unstable, the Poincaré–Bendixson theorem guarantees the existence of at least one stable limit cycle within the trapping region [24]. When multiple fixed points occur in the system, they are introduced in pairs through saddle-node bifurcations. Due to the constraints of nullcline shape, the slope of N_N will be negative when evaluated at (at least) one of these fixed points, thereby implying that at least one fixed point must be stable. In the case of single or multiple stable fixed points, at least part of the basin of attraction of each stable fixed point must lie within the trapping region. Although ultradian rhythms may be modulated by factors such as sleep deprivation, depression, pharmacologic manipulation, or time of day, the existence of ultradian rhythms in human sleep is remarkably robust to significant perturbations [50, 5, 18, 13, 33]. Therefore, even if a stable limit cycle coexists with a stable fixed point, we would expect the robustness of the observed ultradian oscillation

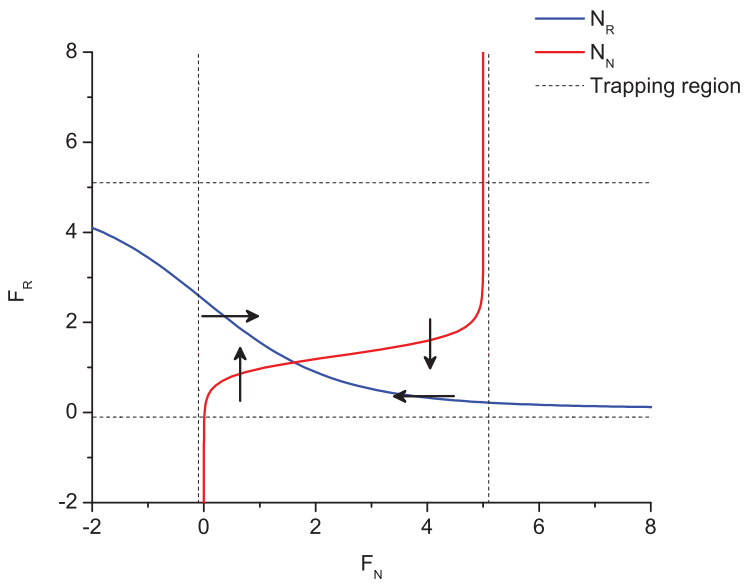

Figure 2. *In the (F_N, F_R) phase plane of the RI model, the nullclines N_N (blue) and N_R (red) divide the horizontal and vertical components of the vector field, respectively. Given their shapes and relative configurations, these nullclines must intersect at least once; such an intersection point is a fixed point of the system. The trapping region (dashed lines) defines a boundary along which the vector field is inward-pointing.*

to be compromised in the presence of stochastic input.

Thus, we conclude that the absence of stable fixed points in the trapping region is a necessary and sufficient condition for robust cycling in the RI network. This argument, relying on properties of the phase plane, is analogous to that given by Wilson and Cowan for the existence of limit cycles in their network of excitatory and inhibitory neuronal populations [51].

3.2. Investigating the robustness of cycling in the RI model. Given the condition for robust ultradian cycling established in the previous section, we can evaluate the effect on cycling of the coupling ($g_{R,N}$ and $g_{N,R}$) and auto-effect ($g_{R,R}$ and $g_{N,N}$) parameters by examining the changing number and stability of fixed points as parameters vary. Starting with a set of parameters that produces a robust ultradian rhythm ($g_{R,R} = 6$; $g_{N,R} = -7$; $g_{R,N} = 7$; $g_{N,N} = -1$), we systematically vary each pair of parameters to investigate sensitivity of cycling to individual parameters and compensatory effects that influence the existence of cycling solutions (Figure 3). We focus on the existence of cycling solutions without placing constraints on the period of the oscillation. For each parameter set, the number and stability of fixed points are determined, and the stable model solution is identified. If there are no stable fixed points, the above arguments establish the existence of a stable limit cycle solution. If there are stable fixed points, the firing rates of each population approach either a high ($> \theta_R$ Hz) or low ($< \theta_R$ Hz) steady state. In some narrow regions of parameter space, two different fixed points are stable, and bistability of steady-state solutions exists.

Although coupling parameters are not defined with respect to a specific, measurable scale, we assume that they do not vary over many orders of magnitude. If modest variation of a parameter destroys cycling, then we interpret this as a lack of robustness with respect to

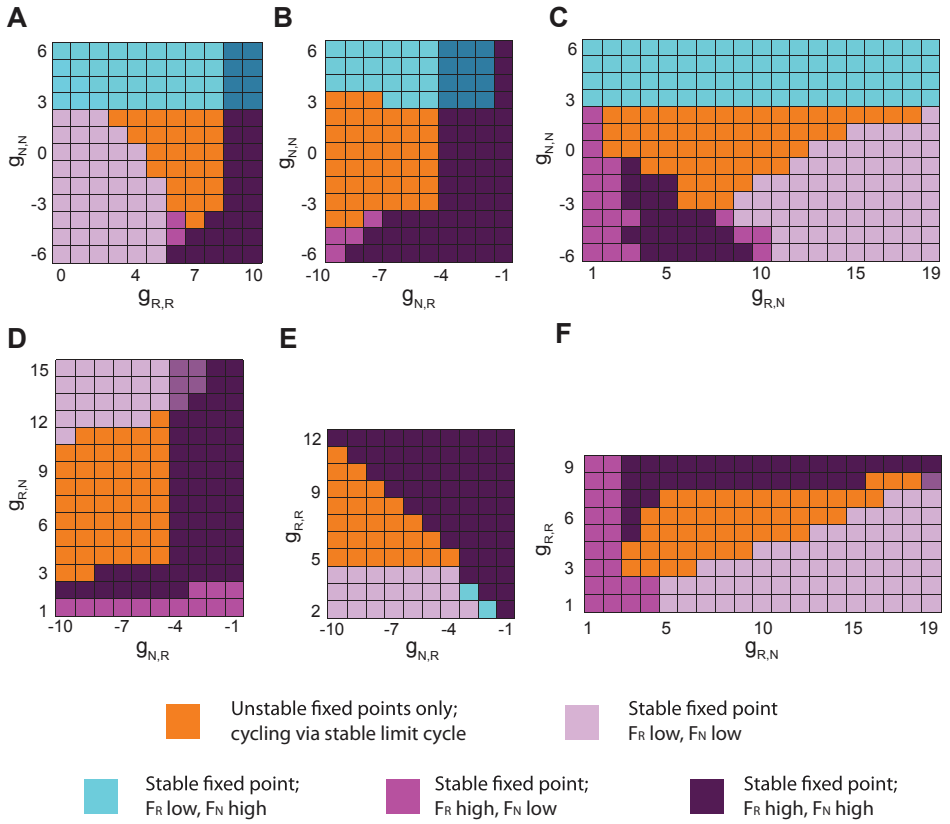

Figure 3. *In the RI model, cycling is relatively robust to variations in parameters.* (A–F) *Stable model solutions obtained under pairwise variation of the auto- ($g_{R,R}$ and $g_{N,N}$) and cross-effect ($g_{R,N}$ and $g_{N,R}$) parameters with all other parameter values fixed. In stable fixed point solutions, each neuronal population approaches a steady-state value that corresponds to a high ($> \theta_R$ Hz) or low ($< \theta_R$ Hz) firing rate. Color indicates type of stable solution: Orange = stable limit cycle, lavender = stable fixed point with F_R and F_N at low values, cyan = stable fixed point with F_R at low value and F_N at high value, magenta = stable fixed point with F_R at high value and F_N at low value, and dark purple = stable fixed point with F_R and F_N at high values. Parameter regions with blended colors indicate bistability of fixed point model solutions: Dark blue = bistability between F_R low/F_N high and F_R high/F_N high stable fixed points; light blue = bistability between F_R low/F_N low and F_R low/F_N high; and purple = bistability between F_R low/F_N low and F_R high/F_N high. Default parameter values are $g_{R,R} = 6$; $g_{N,R} = -7$; $g_{R,N} = 7$; and $g_{N,N} = -1$.*

that parameter. If cycling is robust to large variation in a given parameter, then we show the cycling region over a reasonable range of the parameter and do not specify the boundary of the cycling region with respect to that parameter. For example, in Figure 3B, cycling persisted for very large negative values of $g_{N,R}$, and so the cycling region is portrayed as unbounded with respect to $g_{N,R}$.

Generally, in the RI network, cycling depends on the ability of the R population to activate in the absence of inhibition, and the dependence of N population activation on excitation from R. Cycling occurs through the following sequence of events: when N is inactivated, R activates and drives activation of N through excitation. Inhibition from N suppresses R, and the resulting decay in excitation from R causes N to inactivate. Inactivation of N releases R

from inhibition, thereby allowing R to activate and repeat the cycle.

This pattern of alternating activity of the R and N populations is sensitive to the auto-effect parameters $g_{N,N}$ and $g_{R,R}$ as they influence the ability of each population to activate or inactivate in the absence of input from the other population. When self-excitation of the N population is strong ($g_{N,N}$ large and positive), N is persistently active, and the resulting persistent inhibition to the R population induces a stable fixed point with F_N at a high value and F_R at a low value (cyan region of Figure 3, panels A, B, and C). Similarly, strong self-excitation of the R population ($g_{R,R}$ large and positive), leads to persistent R activation, even in the presence of inhibition from N, and its persistent excitatory input to the N population induces a stable fixed point with both F_R and F_N at high levels (dark purple regions in Figure 3, panels A, E, and F). For low, positive $g_{R,R}$, R may not activate at all, leading to a stable fixed point at low levels for both F_R and F_N (lavender regions in Figure 3, panels A, E, and F). Although cycling can exist when N is self-inhibiting ($g_{N,N}$ negative), very negative $g_{N,N}$ values maintain N inactivation and induce stable fixed points with F_N at low levels (magenta and lavender regions in Figure 3, panels A, B, and C).

Interestingly, changes in other parameters can compensate for the negative impact of these auto-effect parameters on cycling, as indicated by diagonal boundaries of the cycling parameter regions (orange regions in Figure 3, panels A, E, and F). Cycling can occur when self-excitation to R, $g_{R,R}$, is increased if the inhibition from N to R, $g_{N,R}$, is also stronger ($g_{N,R}$ more negative) to enable inactivation of the R population (Figure 3E). Loss of cycling due to a decrease in $g_{R,R}$ is offset by weaker excitation from R to N, $g_{R,N}$, which delays N activation, thereby allowing R to activate fully before it is inhibited by N (Figure 3F). A decrease in $g_{R,R}$ can also be offset by an increase in $g_{N,N}$ which allows N to activate despite the weaker excitation from R (Figure 3A). In this case, as long as $g_{N,N}$ is not too high, N will not be able to maintain activation when R is inhibited, and cycling will occur.

Cycling is also sensitive to both high and low values of $g_{R,N}$, the strength of excitation from R to N. High values of $g_{R,N}$ produce a stable fixed point with both F_R and F_N at low levels due to a balance of strong inhibition to R and weak excitation to N (lavender regions in Figure 3, panels C, D, and F). Specifically, feedback inhibition from N keeps R at a low level, and N cannot fully activate due to insufficient excitation from R. Cycling can be rescued from this balanced state by increasing $g_{N,N}$, which promotes full N activation (Figure 3C). When $g_{R,N}$ is low, N can activate only partially, and the resulting low level of inhibition is unable to suppress R, thereby producing stable fixed points at high values of F_R (dark purple and magenta regions in Figure 3, panels C, D, and F).

Cycling is least sensitive to strong inhibition from N to R, $g_{N,R}$, and the cycling region extends to very large negative values of this parameter (orange regions in Figure 3, panels B, D, and E). This insensitivity indicates that the maximal strength of inhibition to R is less important to cycling than the eventual release of this inhibition. On the other hand, cycling does not occur if $g_{N,R}$ is too weak, and N is not able to suppress R. In this case, a stable fixed point with both F_R and F_N at high levels is induced (dark purple regions in Figure 3, panels B, D, and E).

These predicted dependencies on coupling parameters may be interpreted in terms of the underlying physiology and effects on REM sleep cycling to suggest targets for further experimental investigation of the generation of ultradian cycling (see section 6).

4. Mutual inhibition models.

4.1. REM sleep homeostatic drive acting on N population (MIHN). With the inclusion of the dynamics of the REM sleep homeostatic drive acting on the N-population, the MI network is a 3D system. The time scale for the REM homeostat, h, is necessarily slower than the time scales governing F_R and F_N (on the order of bout durations as compared to state transition times); thus we can informally decompose the model into a fast subsystem consisting of the equations for F_R and F_N (2.1) and a slow subsystem consisting of the equation for h (2.6) [16, 39]. Model dynamics may then be analyzed in terms of the fast subsystem with the slow variable h considered as a parameter with values between $[0, 1]$.

With this fast-slow decomposition, cycling can be understood as movement around a hysteresis loop. In the default model parameter set, computing the bifurcation diagram of the fast subsystem, with respect to h as the bifurcation parameter, reveals a Z-shaped curve of fixed point solutions (Figure 4A). We will call these fixed points of the fast subsystem *conditional fixed points* of the 3D model. For high and low values of h, single stable conditional fixed points exist with low F_R values and high F_R values, respectively. In some parameter regimes, there is a range of h values associated with a region of bistability between two distinct, stable conditional fixed points. For the default parameters, the saddle-node bifurcations defining this region of bistability occur at $h = 0.193$ and $h = 0.385$. The trajectory of the 3D model (purple curve) will approach one of these stable conditional fixed points as h varies. Under our assumptions of a REM-terminating homeostat, h increases toward 1 when $F_R > \theta_R$ and the trajectory tracks the upper stable branch of the fixed point curve, corresponding to the REM state (blue), until h increases past the right saddle-node point. At these higher h values, the only stable conditional fixed points occur on the lower branch of the curve, corresponding to the NREM state (red), and the trajectory jumps down to approach them. With the jump down, F_R falls below θ_R, thereby causing h to decrease toward zero. The trajectory tracks the stable conditional fixed points on the lower branch of the curve until h decreases below the left saddle-node point and the trajectory jumps back up to the upper stable branch. Thus, the slow, repeated reversals of the dynamics governing h drive the trajectory of the full model system around this region of bistability to produce a stable, periodic oscillation (Figure 4C).

Equivalently, we can track the cycling trajectory of the 3D network in the (F_N, F_R) phase plane of the fast subsystem (Figure 4B). Since the F_N equation depends on h, through modulation of the parameter β_N, the N-nullcline varies with h, and we need to consider the family of N-nullclines $N_{N,h}$ for fixed values of h in the interval $[0, 1]$. Intersection points of the F_R nullcline, N_R, with the nullclines in the family $N_{N,h}$, correspond to the conditional fixed points described by the Z-shaped curve of fixed point solutions to the fast subsystem (Figure 4A). For any fixed value of h, $N_{N,h}$ is continuous and, as a result of their relative configurations, intersects the F_R nullcline N_R, so conditional fixed points will always exist. In the h interval of bistability, the nullclines have three intersection points, two of which are stable. As h increases when $F_R > \theta_R$, the F_N nullcline associated with h will transition slowly through curves in the family $N_{N,h}$ to approach $N_{N,1}$ (upward in the phase plane), and the trajectory will track the stable conditional fixed point with F_R value above θ_R (corresponding to the REM state) at the intersection of these nullclines. In the default parameter set, this

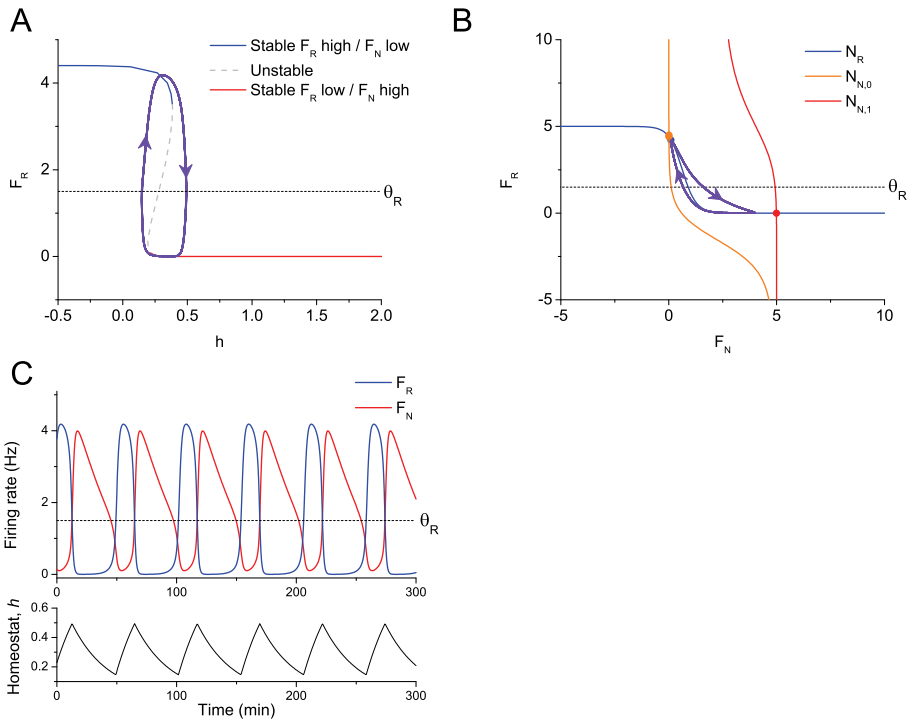

Figure 4. *Understanding hysteresis-loop cycling in the MI model with h acting on the N population (MIHN).* A. *Fast-slow decomposition allows visualization of cycling as a hysteresis-loop trajectory (purple) defined by $h(t)$ movement across saddle-node bifurcations (at $h = 0.193$ and $h = 0.385$) in the Z-shaped bifurcation curve of the fast subsystem (2.1) computed with respect to parameter h. Under our assumptions of a REM-terminating homeostat, h increases toward 1 when $F_R > \theta_R$ (dotted line) and decreases toward 0 when $F_R < \theta_R$.* B. *In the (F_N, F_R) phase plane, the cycle trajectory (purple) tracks conditional fixed points at the intersection of the family of N nullclines $N_{N,h}$ with the R nullcline N_R (blue); the nullclines $N_{N,0}$ (orange) and $N_{N,1}$ (red) define the extreme elements of this family.* C. *Plotting the trajectory in time shows the regular oscillation in both F_N (red) and F_R (blue) and its relationship to the alternating activity of h (lower panel).*

conditional fixed point will disappear in a saddle-node bifurcation at $h = 0.385$, and the trajectory will jump to the other stable fixed point with F_R value below θ_R (corresponding to the NREM state). When the F_R component of the trajectory crosses θ_R, the h dynamics will reverse: h will decrease toward 0, and the F_N nullcline associated with h will slowly transition through the family of curves $N_{N,h}$ to approach $N_{N,0}$ (downward in the phase plane). The trajectory then tracks the low F_R stable conditional fixed point at the intersection of these nullclines until a saddle-node bifurcation occurs at $h = 0.193$, at which point it jumps to the high F_R stable conditional fixed point to complete the cycle.

4.1.1. Deriving numerical criteria for the existence of cycling in the MIHN model.

There are two general mechanisms associated with the loss of hysteresis-loop cycling in this system: the system may approach a stable fixed point of the full 3D model, or the h dynamics may trap the system near the threshold value $F_R = \theta_R$. In terms of the fast subsystem bifurcation diagram, these mechanisms can be understood as follows:

1. If a stable branch of the Z-shaped bifurcation curve (possibly deformed by parameter variation) intersects the line $h = 0$ below the threshold $F_R = \theta_R$ or intersects the line $h = 1$ above the threshold $F_R = \theta_R$, the intersection point will be a stable fixed point of the full 3D system. We call this solution a *system fixed point*, and the model trajectory will approach the steady-state values associated with this stable fixed point (Figure 5C).
2. If a stable branch of the (possibly deformed) Z-shaped bifurcation curve intersects the threshold, $F_R = \theta_R$, the system will enter into an oscillation about this point (Figure 5E). We will refer to this solution as a stable *threshold fixed point*.

To investigate the robustness of cycling in the MI model with h acting on the N population, we determined an efficient method to identify the existence of hysteresis-loop cycling that does not require computation of bifurcation diagrams for each parameter set. As in the RI case, consideration of the phase plane provided the desired numerical criteria.

From the full 3D model system, we can define the piecewise h-nullsurface, N_h, obtained by setting $h' = 0$:

$$N_h = \left\{ \begin{array}{ll} \{F_N, F_R, h\} \mid h = 1 & \text{when } F_R > \theta_R \\ \{F_N, F_R, h\} \mid h = h* & \text{when } F_R = \theta_R \\ \{F_N, F_R, h\} \mid h = 0 & \text{when } F_R < \theta_R \end{array} \right\} \tag{4.1}$$

for $h* = \tau_1/(\tau_1 + \tau_2)$.

Given the h-dependence of the F_N equation, the N-nullsurface is piecewise defined as follows:

$$N_N = \left\{ \begin{array}{lll} N_{N,1} & = \{F_N, F_R, h\} \mid F_N' = 0, h = 1 & \text{when } F_R > \theta_R \\ N_{N,h*} & = \{F_N, F_R, h\} \mid F_N' = 0, h = h* & \text{when } F_R = \theta_R \\ N_{N,0} & = \{F_N, F_R, h\} \mid F_N' = 0, h = 0 & \text{when } F_R < \theta_R \end{array} \right\}. \tag{4.2}$$

The R-nullsurface, $N_R = \{\{F_N, F_R, h\} \mid F_R' = 0\}$, has no explicit h-dependence and thus is continuous.

Using this construction, the 3D system can be analyzed in the 2D (F_N, F_R) phase plane. The assumption that h has attained a steady-state value ($h = 0$, 1, or $h*$) is built into the specification of pieces of N_N, so an intersection point of the piecewise N_N with N_R in the (F_N, F_R) phase plane corresponds to a fixed point of the full 3D system, i.e., a system fixed point. Since N_N is discontinuous, N_N and N_R may fail to intersect, perhaps allowing for the existence of hysteresis-loop cycling. However, if a system fixed point exists and is stable, nearby trajectories will approach it. Since we are interested in cycling in the presence of significant stochastic input, even a small basin of attraction associated with a stable system fixed point will compromise the robustness of ultradian cycling. Therefore, we will consider the absence of a stable system fixed point to be a necessary condition for hysteresis-loop cycling.

Relating this phase plane analysis to the bifurcation diagram of the fast subsystem, the existence of stable system fixed points corresponds to an intersection of a stable branch of the Z-shaped curve of fixed points with the line $h = 0$ for $F_R < \theta_R$ or the line $h = 1$ for $F_R > \theta_R$. Stable system fixed points may arise from parameter variation resulting in several

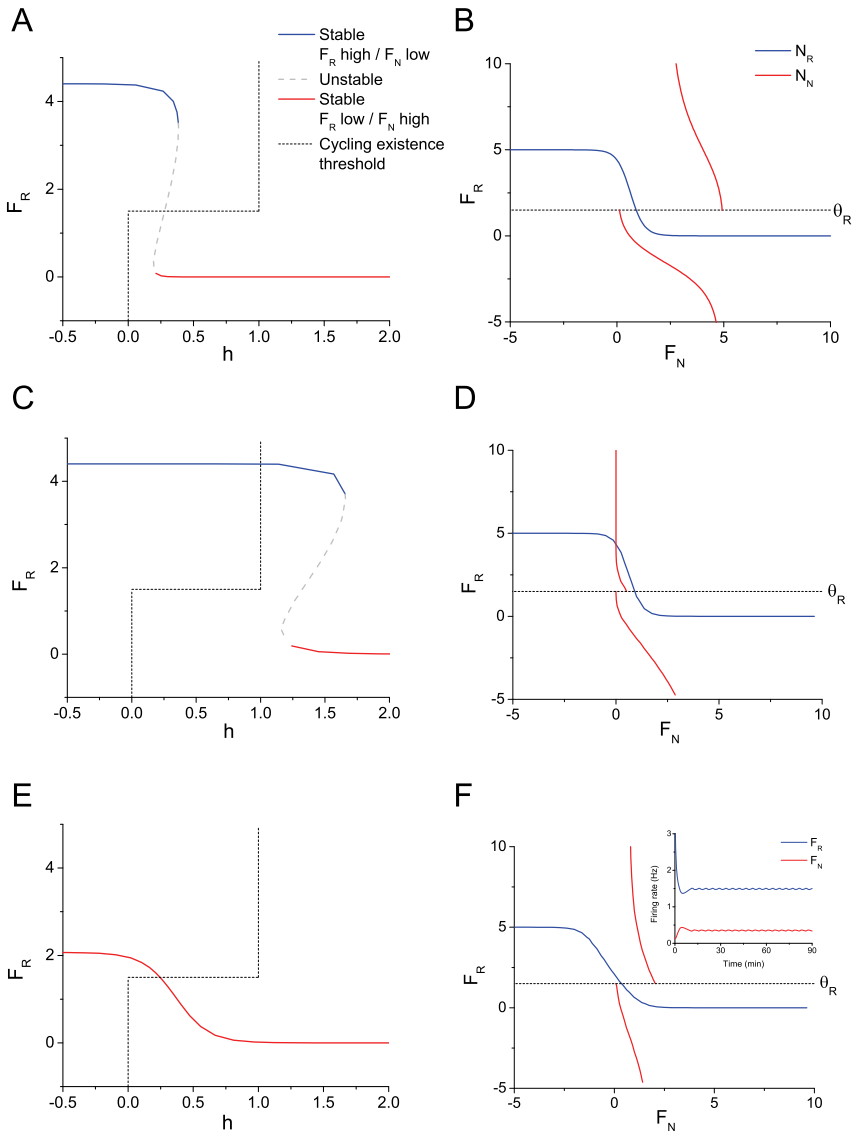

Figure 5. *In the MIHN model, hysteresis-loop cycling* (A,B) *can be lost through the introduction of a system fixed point* (C,D) *or of a stable threshold fixed point* (E,F). A. *Bifurcation curve of the fast subsystem* (2.1) *with default parameters* ($g_{R,R} = 0$; $g_{N,R} = -4$; $g_{R,N} = -1.5$; $g_{N,N} = 0$) *with respect to the parameter* h *is a Z-shaped curve of steady state solutions in which the two stable branches (solid blue and red) are separated by an unstable branch (gray, dashed). System or threshold fixed points can be visualized by an intersection of a stable branch of the Z-shaped curve with the cycling existence threshold curve (gray, dotted) defined by* (4.3). B. (F_N, F_R) *phase plane showing piecewise* N_N *nullcline (red, formed from* $N_{N,0}$ *and* $N_{N,1}$*) and continuous* N_R *nullcline (blue) for default parameters.* C. *With different values of the coupling and auto-effect parameters, a system fixed point appears as the intersection of a stable branch of the bifurcation diagram of the fast subsystem (blue) with the cycling existence threshold curve* ($g_{R,R} = 0$; $g_{N,R} = -4$; $g_{R,N} = -5$; $g_{N,N} = -6$). D. *The system fixed point is indicated by the intersection of* N_R *and* $N_{N,1}$. E. *By varying coupling and auto-effect parameters, the bifurcation curve becomes completely stable, and a stable threshold fixed point occurs at the intersection with the horizontal portion of the cycling existence threshold curve* ($g_{R,R} = -1.5$; $g_{N,R} = -4$; $g_{R,N} = -1.5$; $g_{N,N} = -3$). F. *The existence of the stable threshold fixed point is not apparent in the configuration of nullclines in the* $F_N - F_R$*-phase plane, but the* h *dynamics trap the system trajectory in an oscillation about this threshold fixed point (inset).*

qualitatively different changes to the Z-shaped bifurcation curve. In one such change, the region of bistability is preserved, but the saddle-node points of the Z-shaped curve occur outside the h-interval $[0, 1]$ (see, for example, Figure 5C). If the leftmost saddle-node point is below $h = 0$, the system fixed point will occur on the $N_{N,0}$ piece of the N-nullcline; similarly, if the rightmost saddle-node point is above $h = 1$, the system fixed point will occur on the $N_{N,1}$ piece of the N-nullcline.

Although the existence of stable system fixed points represents an important mechanism whereby cycling fails, the absence of stable system fixed points is not a sufficient condition for cycling in this network. Even when system fixed points fail to exist, the dynamics of h may cause the trajectory to oscillate about a stable conditional fixed point with its F_R-coordinate at θ_R, i.e., a threshold fixed point. To understand the role of the h dynamics in the existence of cycling, we must consider the behavior of the trajectory as F_R crosses the threshold. If the threshold fixed point is an unstable fixed point in the 2D system, the F_R coordinate of the trajectory will cross this value only as the trajectory jumps between stable conditional fixed points. Although crossing the threshold will cause the h dynamics to reverse, the separation of time scales between the fast and slow subsystems allows for a relatively quick transition. However, if the threshold fixed point is a stable conditional fixed point in the 2D system, then the trajectory will slowly approach the threshold fixed point as h varies. As the trajectory passes through the stable threshold fixed point, h reverses, and the trajectory is forced to track back along the same path. It then crosses the threshold in the opposite direction, and, again, the h dynamics will reverse. This behavior will produce oscillations around the threshold fixed point, and the trajectory will be trapped near the threshold fixed point even though this fixed point is not a stable fixed point of the 3D system. These oscillations will depend sensitively on the time scale of the h dynamics and the time step used in numerical integration since they are constrained by small movements of F_R around θ_R. As discussed in section 6, the occurrence of a stable threshold fixed point is a consequence of the mathematical formulation of the REM sleep homeostatic drive rather than a change in the bifurcation structure of the system, and its effect on network dynamics should be interpreted with care.

In the bifurcation diagram computed with respect to h, the existence of stable threshold fixed points corresponds to an intersection of a stable branch of the Z-shaped curve of fixed points of the 2D system with the line associated with the threshold, θ_R. Given the constraints on the Z-shaped curve, some part of the curve will always intersect this threshold. However, when the curve is a true Z-shape with a region of bistability, this intersection point tends to lie on the unstable branch of the Z. As coupling and auto-effect parameters are varied, stable threshold fixed points can be introduced by two different mechanisms. One mechanism occurs when the bifurcation curve has the proper Z-shape and bistability of stable steady states to support hysteresis-loop cycling, but one of the stable steady-state branches crosses $F_R = \theta_R$ within the interval $0 \leq h \leq 1$. Another mechanism by which a stable threshold fixed point is introduced occurs when the bifurcation curve is distorted so that the bistability region of stable steady states is lost, and all steady-state solutions on the curve are stable, including the steady state at $F_R = \theta_R$ (as shown in Figure 5E). We note that a loss of the region of bistability will necessarily destroy hysteresis cycling through the creation of either a system fixed point or a stable threshold fixed point.

In summary, existence of hysteresis-loop cycling can be determined in the bifurcation diagram of the 2D fast subsystem by the absence of intersection of any stable branch of conditional fixed points with the piecewise step curve defined as follows (dashed line in Figure 5):

$$\mathcal{C} = \left\{ \{h, F_R\} \;\middle|\; \begin{array}{lll} h = 0 & \text{and} & F_R < \theta_R \\ 0 < h < 1 & \text{and} & F_R = \theta_R \\ h = 1 & \text{and} & F_R > \theta_R \end{array} \right\}. \tag{4.3}$$

We refer to this curve as the cycling existence threshold. Equivalently, and more efficiently, existence of hysteresis-loop cycling can be determined in the (F_N, F_R) phase plane if there are no intersection points of N_R with the piecewise N_N and the conditional fixed points with values $F_R = \theta_R$ are unstable. We numerically implement this latter test to analyze the robustness of cycling in the MI models.

4.1.2. Investigating the robustness of cycling in the MIHN model. As in the RI model, we investigated the robustness of cycling regimes by establishing a set of parameters that produces a robust ultradian rhythm ($g_{R,R} = 0$; $g_{N,N} = 0$; $g_{N,R} = -4$; $g_{R,N} = -1.5$). Then we systematically vary the parameters associated with the strength of both auto-effects ($g_{R,R}$ and $g_{N,N}$) and coupling ($g_{R,N}$ and $g_{N,R}$). We identify parameter regimes that produce robust ultradian cycling, and we observe the parameter changes that result in failure of cycling as a result of stable system fixed points or stable threshold fixed points (Figure 6). In some narrow parameter regions, two system fixed points are stable, and bistability of solutions occurs. As previously noted, we focus on the existence of cycling solutions without placing constraints on the period of the oscillation.

As in the robustness analysis of the RI model, we assume that coupling parameters do not vary over many orders of magnitude, and, if the cycling regime is robust to large variation in a given parameter, then we show the cycling region over a reasonable range of the parameter and do not specify the boundary of the cycling region with respect to that parameter.

Since the mechanism for cycling in the MI model depends on the REM homeostat, the specific parameter regions where cycling exists also depend on the choice of parameters describing the REM homeostat. We have defined the REM homeostat to have lower and upper saturation levels at 0 and 1, respectively. The values of these saturation levels affect the values of the coupling and auto-effect parameters where cycling is lost. However, they do not affect the qualitative change in dynamics as the parameters are varied. Thus, if the homeostat saturation levels were different, the cycling parameter regions would contract or expand, but the model solutions at the boundaries of the cycling regions would not change. The existence of stable threshold fixed points is particularly sensitive to the specification of the REM sleep homestatic drive (as discussed in section 6.3). Since this mechanism for the loss of cycling does not correspond to a stable system fixed point and may occur as a result of h dynamics even when the general bifurcation structure of the system is conducive to hysteresis-loop cycling, we designated parameter regions associated with stable threshold fixed points with a hatched orange pattern in Figure 6.

Auto-effects on the R population, governed by $g_{R,R}$, can destroy cycling by affecting the ability of R to activate or inactivate. High R self-excitation ($g_{R,R}$ large and positive) allows maintained R activation even when N is activated, thereby producing a system fixed point

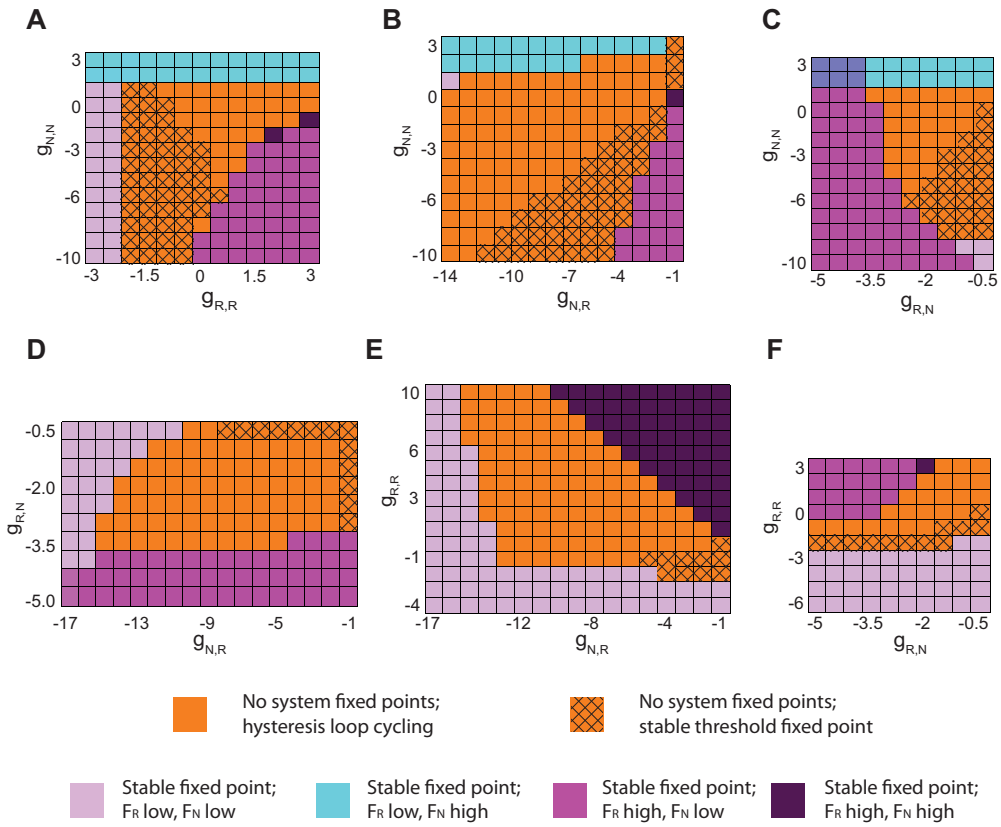

Figure 6. *In the MIHN model, cycling is relatively robust to variations in parameters. Panels* A–F *correspond to the pairwise variation of the auto- ($g_{R,R}$ and $g_{N,N}$) and cross-effect ($g_{R,N}$ and $g_{N,R}$) parameters with all other parameter values fixed. Default parameter values are $g_{R,R} = 0$; $g_{N,N} = 0$; $g_{N,R} = -4$; and $g_{R,N} = -1.5$. Cycling (orange), as well as failure of cycling due to threshold fixed points (orange, hatched) or stable system fixed points, is depicted. As in Figure 3, color indicates type of stable solution: Lavender = stable system fixed point with F_R and F_N at low ($< \theta_R$) values, cyan = stable system fixed point with F_R at low value and F_N at high ($> \theta_R$) value, magenta = stable system fixed point with F_R at high value and F_N at low value, and dark purple = stable system fixed point with F_R and F_N at high values. In the case of bistability between different system fixed points, a blend of the colors associated with each fixed point is presented: Light blue = bistability between F_R low/F_N low and F_R low/F_N high; and bright purple = bistability between F_R high/F_N low and F_R low/F_N high. If a cycling region is depicted as unbounded with respect to a parameter, then cycling persisted robustly over large ranges of that parameter.*

with both F_R and F_N at high values (dark purple regions in Figure 6, panels A, E, and F). Similar to the RI network, this mechanism for the loss of cycling can be offset by stronger inhibition from N to R ($g_{N,R}$ more negative) which promotes the suppression of R when N activates (diagonal boundary with dark purple region in Figure 6E). High R self-excitation may also lead to a system fixed point with F_R at a high value and F_N at a low value (magenta regions in Figures 6A and 6F) if the REM homeostat saturates due to persistent R activation yet is unable to activate N. This may occur when N self-inhibition is high ($g_{N,N}$ negative) or the inhibition from R to N is strong ($g_{R,N}$ more negative). This mechanism for loss of cycling can be offset by increasing $g_{N,N}$ or $g_{R,N}$ (diagonal boundary with magenta region in Figures

6A and 6F, respectively).

When self-excitation to the N population is high ($g_{N,N}$ large and positive), N can remain activated when the homeostatic drive saturates at its maximal level, thereby inducing a system fixed point with F_N at a high level and F_R at a low level (cyan regions in Figure 6, panels A, B, and C). Cycling is lost to a system fixed point with F_R high and F_N low when the inhibition from R to N, governed by $g_{R,N}$, is too strong ($g_{R,N}$ more negative, magenta regions in Figure 6, panels C, D, and F). In this case, R can remain activated because its strong inhibition blocks the homeostatic release of N. Cycling is least sensitive to the strength of inhibition from N to R, $g_{N,R}$ and is lost for very negative values to a system fixed point with both F_R and F_N at low values (lavender regions in Figures 6D and 6E). At these values, the homeostat has inactivated N to a minimal, but nonzero, level which provides sufficient inhibition to suppress R activation. From this state, cycling can be restored by increasing $g_{R,R}$, and thus promoting R activation (diagonal boundary with lavender region in Figure 6E), or making the inhibition from R to N stronger ($g_{R,N}$ more negative), thereby allowing partial R activation to suppress N and thus promote its own release from inhibition (diagonal boundary with lavender region in Figure 6D).

Inhibitory auto-effects on either population can cause a loss of cycling by the introduction of a stable threshold fixed point (orange hatched regions on Figure 6, panels A, B, C, E, and F). In the MIHN model, self-inhibition can lead to the elimination of the region of bistability in the Z-shaped bifurcation curve; the curve becomes completely stable with a single stable fixed point of the 2D fast subsystem associated with each value of h, and, specifically, a single stable fixed point at the threshold value $F_R = \theta_R$ (as illustrated in Figure 5E). The bistable region of the Z-shaped bifurcation curve, which supports the hysteresis-loop cycling mechanism, is generated by the different levels of homeostatically regulated excitability of the N population necessary for its inactivation when the R population is off and for its activation when the R population is activated. When the R population is self-inhibitory ($g_{R,R}$ negative), the maximal F_R level is lower, and thus N receives less cross-inhibition. Activation of N can then occur at lower levels of the homeostat h, and the bistable region can be eliminated by the saddle-node point at high h values moving to lower h values and eventually disappearing. When the N population is self-inhibitory ($g_{N,N}$ negative), this auto-effect works in conjunction with the homeostatic drive to promote N inactivation, and N is inactivated at higher levels of the homeostat h. In this case, the bistable region of the bifurcation curve can be eliminated by the saddle-node point at lower h values moving to higher h values and eventually disappearing.

The physiological implications of these parameter dependencies for ultradian cycling are addressed in section 6.

4.2. REM sleep homeostatic drive acting on R-population (MIHR). In the MI model with the REM-terminating homeostatic drive acting on the REM-promoting R population, we can apply the same fast-slow decomposition described above to analyze cycling as movement around a hysteresis loop defined by the bifurcation diagram of the fast (F_N, F_R) subsystem with respect to the bifurcation parameter h (Figure 7A, C). We can also equivalently track the trajectory in the (F_N, F_R) phase plane as it follows the slowly varying stable conditional fixed points at the intersections of the continuous N-nullcline N_N and the family of R-nullclines $N_{R,h}$ as $h(t)$ varies between 0 and 1 (Figure 7B). However, the site of action of the homeostat

represents an important difference between systems. Since the threshold for determining h-dynamics depends on F_R, cycling in this case is driven by a direct interaction between F_R and h: a sufficiently low value of h will allow F_R to activate, but this activation will cause h to increase and eventually terminate activity in F_R. This mechanism does not depend on activity in F_N. Thus, although inhibition from F_N may contribute to terminating activity in F_R and producing cycling, it is not a necessary component of the cycling mechanism. For example, in parameter regimes where strong self-excitation of the N population keeps F_N at high levels, oscillations in F_R may occur while F_N is fixed at a stable high value (Figure 7D).

4.2.1. Deriving numerical criteria for the existence of cycling in the MIHR model. In the MIHR model, we observe the same mechanisms for loss of cycling that were described for the MIHN model, namely, the existence of stable system or stable threshold fixed points. For the full 3D model, we use the piecewise h-nullsurface (4.1) to compute a piecewise R-nullcline, N_R, in the (F_N, F_R) phase plane (Figure 7B; solid portions of nullclines represent N_R; dash-dot portions are not included in N_R but are shown for reference). System fixed points are defined as intersection points of the continuous N-nullcline with the piecewise R-nullcline in the (F_N, F_R) phase plane. Threshold fixed points are defined as stable conditional fixed points with $F_R = \theta_R$. We determine existence of hysteresis-loop cycling as we did for the MIHN model by first conducting a numerical search for stable system fixed points. If no stable system fixed points are present, then we search for stable threshold fixed points. Finally, we distinguish between cases in which F_N is participating in the robust cycling of F_R and cases when F_N is fixed at a constant or near-constant value. We define the parameter regimes in which both F_R and F_N oscillate to be associated with robust ultradian cycling. However, it is important to note that, at the behavioral level, isolated cycling in F_R may be indistinguishable from cycling in F_R and F_N.

4.2.2. Investigating the robustness of cycling in the MIHR model. As in the previous models, we investigated the robustness of cycling regimes by establishing a set of coupling parameters that produces a robust ultradian rhythm ($g_{R,R} = 0$; $g_{N,N} = 0$; $g_{N,R} = -2$; $g_{R,N} = -2$). Then we systematically vary the parameters associated with the strength of both auto-effects ($g_{R,R}$ and $g_{N,N}$) and coupling ($g_{R,N}$ and $g_{N,R}$). We identify parameter regimes that produce robust ultradian cycling and that result in failure of cycling as a result of stable system fixed points, stable threshold fixed points, bistability of system fixed points, or nonparticipation of F_N (Figure 8). As in the previous cases, we focus on the existence of cycling solutions without placing constraints on the period of the oscillation.

As before, we assume that coupling parameters do not vary over many orders of magnitude, and, if the cycling regime is robust to large variation in a given parameter, then we show the cycling region over a reasonable range of the parameter and leave the boundary unspecified. Since the regions of cycling were so much more constrained in this case, the only region in which cycling is unbounded with respect to parameter variation occurs in Figure 8B.

Similar to the MIHN model, we have bounded our homeostat between 0 and 1. Again, we note that the values of these saturation levels affect the values of the auto-effect and coupling parameters where cycling is lost. However, they do not affect the qualitative change in dynamics as the parameters are varied. Thus, if the homeostat saturation levels were different, the cycling parameter regions would contract or expand, but the model solutions

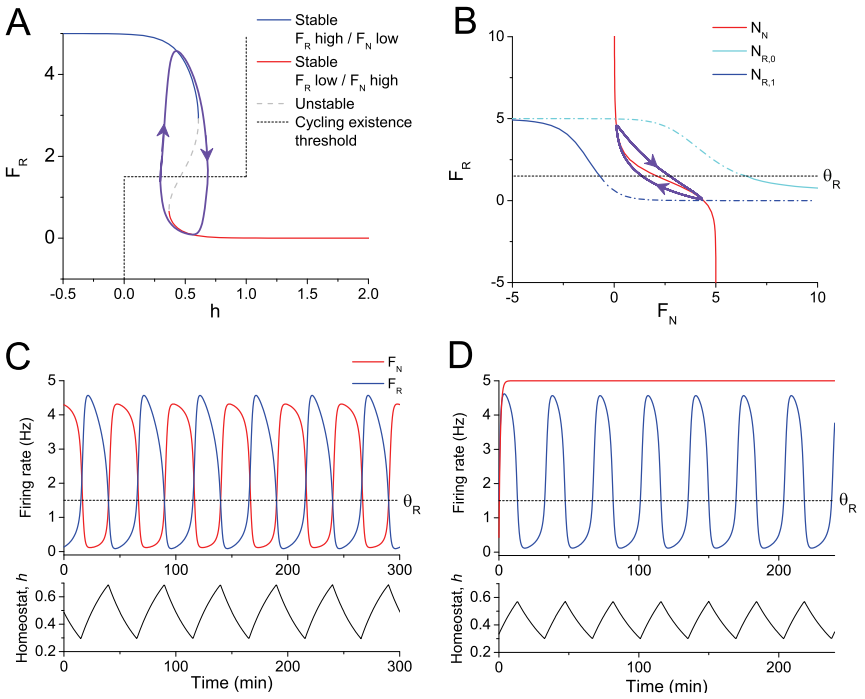

Figure 7. *Understanding the hysteresis-loop oscillation in the MI model with h acting on the R population (MIHR).* A. *As in the MIHN system, fast-slow decomposition shows cycling as a hysteresis-loop trajectory (purple) defined by movement across saddle-node bifurcations in the Z-shaped bifurcation curve of the fast subsystem* (2.1) *computed with respect to parameter h ($g_{R,R} = 0$; $g_{N,N} = 0$; $g_{N,R} = -2$; $g_{R,N} = -2$). The cycling existence threshold curve (dotted) is shown for reference. Under our assumptions of a REM-terminating homeostat, h increases toward 1 when $F_R > \theta_R$ (horizontal portion of cycling existence threshold curve) and decreases toward 0 when $F_R < \theta_R$.* B. *In the (F_N, F_R) phase plane, the cycle trajectory (purple) tracks conditional fixed points at the intersection of the family of R nullclines $N_{R,h}$ with the N nullcline N_R (red). The nullclines $N_{R,0}$ (cyan) and $N_{R,1}$ (blue) define the extreme elements of this family, and their solid portions compose the piecewise R nullcline N_R of the full 3D system; the dash-dot portions are included for reference.* C. *Plotting the trajectory in time shows the regular oscillation in both F_N (red) and F_R (blue) and its relationship to the alternating activity of h (lower panel).* D. *In this model, it is possible for cycling to occur in F_R without involving cycling in F_N, i.e., while F_N remains fixed ($g_{R,R} = 2$; $g_{N,N} = 6$; $g_{N,R} = -2$; $g_{R,N} = -2$).*

at the boundaries of the cycling regions would not change. As in Figure 6, we designated parameter regions associated with stable threshold fixed points with a hatched orange pattern in Figure 8.

When the REM sleep homeostatic drive acts on the R population, robust cycling is much more sensitive to changes in any of the auto-effect or coupling parameters than in the RI or MIHN networks (Figure 8). In this network, variations in several parameters can induce a stable system fixed point with F_N at a high level and F_R at a low level (cyan regions in Figure 8, panels A, B, D, E, and F). Self-excitation of the N population ($g_{N,N}$ positive) and sufficiently strong inhibition to the R population ($g_{N,R}$ more negative) can allow F_N to attain its maximal level and force the homeostatic drive to its low saturation level that fails to activate the R population (cyan region in Figures 8A and 8B). This effect can be offset by decreasing the

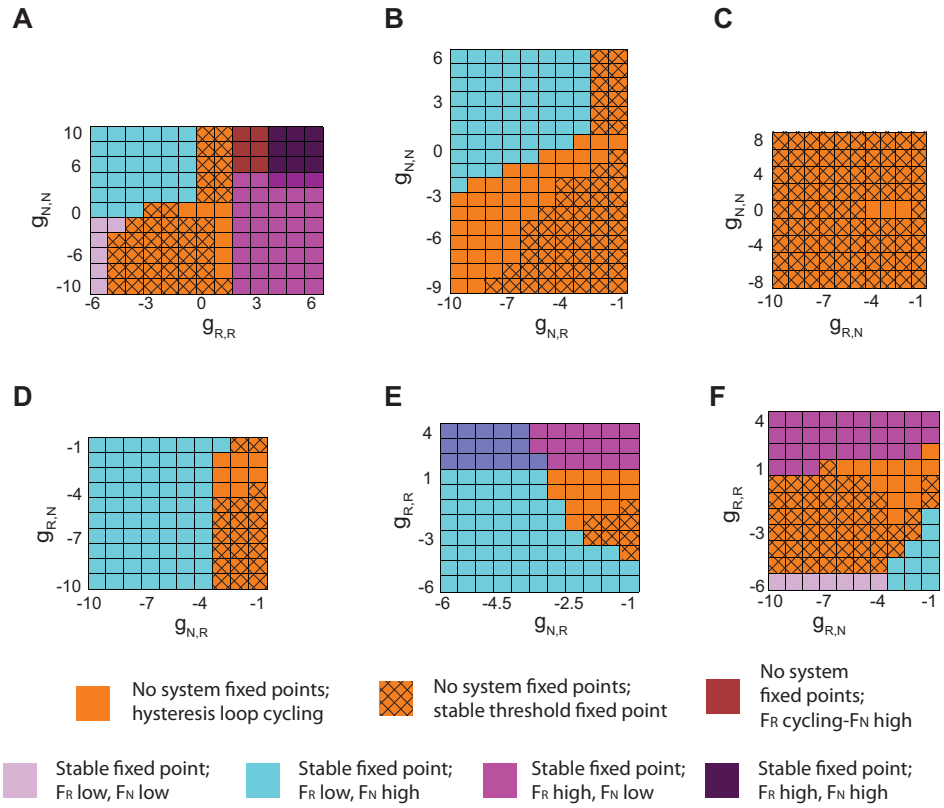

Figure 8. *In the MIHR model, cycling is highly sensitive to variations in parameters. Panels* A–F *correspond to the pairwise variation of two coupling parameters with all other parameters fixed. Default parameter values are* $g_{R,R} = 0$; $g_{N,N} = 0$; $g_{N,R} = -2$; *and* $g_{R,N} = -2$. *Cycling (orange), as well as failure of cycling due to threshold fixed points (orange, hatched) or system fixed points (colors represent same stable solutions as given in Figure 6), is depicted. In the case of bistability between different fixed points, a blend of the colors associated with each fixed point is presented: dark magenta = bistability between* F_R *high/*F_N *low and* F_R *high/*F_N *high; and bright purple = bistability between* F_R *low/*F_N *high and* F_R *high/*F_N *low. If a cycling region is depicted as unbounded with respect to a parameter, then cycling persisted robustly over large ranges of that parameter.*

strength of inhibition from N to R ($g_{N,R}$ less negative), thus enabling homeostatic activation of R (diagonal boundary with the cyan region in Figure 8B). A similar stable system fixed point is induced when the inhibition from N to R is strong ($g_{N,R}$ more negative; cyan regions in Figures 8D and 8E). Again, this inhibition can be sufficiently strong to prevent homeostatic activation of R. In this case, this effect can be offset by making the R population more self-excitatory (increasing $g_{R,R}$) and thus susceptible to homeostatic activation at higher levels of h (diagonal boundary with cyan region in Figure 8E). Finally, strong self-inhibition to R ($g_{R,R}$ negative) can induce the same system fixed point because homeostatic activation of R is terminated before homeostatic saturation (cyan regions in Figure 8, panels A, E, and F).

Self-excitation of the R population ($g_{R,R}$ positive) can destroy cycling by inducing a stable system fixed point with F_R at a high level and F_N at a low level because the homeostatic drive is unable to inactivate R before reaching its upper saturation limit (magenta regions in Figure 8, panels A, E, and F).

As in the MIHN model, cycling can be lost to a stable threshold fixed point when either population is self-inhibitory ($g_{R,R}$, $g_{N,N}$ negative; hatched regions in Figure 8, panels A, B, C, E, and F). Similar to the other model, sufficiently strong self-inhibition leads to the elimination of the bistability region of the Z-shaped bifurcation curve, and the curve becomes completely stable, specifically at the threshold value $F_R = \theta_R$ (similar to Figure 5E). When the N population is self-inhibitory ($g_{N,N}$ negative), the reduced value of F_N in the activated state reduces the amount of inhibition to R, and the homeostatic activation of R can occur at higher values of the homeostat h. Thus, the saddle-node point at lower values of h moves to higher h values and eventually disappears. When the R population is self-inhibitory ($g_{R,R}$ negative), this auto-effect works in conjunction with the homeostatic drive to promote inactivation of R; thus the saddle-node point associated with the transition from high F_R to low F_R (located at a higher h value) can move to a lower h value and disappear.

Self-excitation of the N population ($g_{N,N}$ positive) can introduce a stable threshold fixed point without elimination of the bistability region of the Z-shaped bifurcation curve (hatched regions in Figure 8, panels A, B, and C). In this case, increased $g_{N,N}$ causes the stable solutions of F_R in its inactivated state to attain higher values, specifically values greater than the threshold value of $F_R = \theta_R$. Thus, the lower stable branch of the Z-shaped bifurcation curve can intersect the horizontal portion of the cycling existence threshold curve (4.3). Such higher values of F_R in its inactivated state result from the necessity of generating increased inhibition to N to force its inactivation: the inhibition to N resulting from F_R staying near θ_R remains in balance with a maximally activated F_N and its inhibition to R, to maintain the stable steady state.

Similarly, weak inhibition from R to N, governed by less negative values of $g_{R,N}$, increase F_R values in its inactivated state potentially leading to a stable threshold fixed point (hatched regions in Figure 8, panels C, D, and F). In the same way, decreased efficacy of the inhibitory input to N from R allows an activated F_N and partially activated F_R ($F_R > \theta_R$) to remain in balance in a stable steady state. When inhibition from R to N is strong (more negative $g_{R,N}$; hatched regions in Figure 8, panels C, D, and F), a stable threshold fixed point is introduced by a decrease in F_R values in its activated state. In this case, the REM sleep homeostatic drive can partially inactivate the R population such that $F_R < \theta_R$, but N is unable to activate due to increased efficacy of the inhibitory input. Thus, partially inactivated F_R remains in balance with inactivated F_N to maintain stability of the steady-state solution.

In the MIHR model, we also observe a cycling solution in which F_R alternates between high and low values, and F_N remains constantly activated (Figure 7D and red region in Figure 8A). This solution corresponds to hysteresis-loop cycling around a Z-shaped steady-state bifurcation curve, but, because of the high self-excitation of the N population, both stable branches have high F_N values. In terms of the dynamics, N can remain activated even when inhibitory input from R is maximal. With respect to F_R, the bifurcation curve has a proper Z-shape with a low F_R and a high F_R stable branch and a narrow region of bistability, supporting the hysteresis loop. This region of bistability is generated by self-excitation of the R population, which introduces an additional input to the R population that the REM sleep homeostatic drive must overcome when inactivating R; the self-excitation is absent when R is inactivated and the homeostatic drive is acting to activate R.

The physiological implications for ultradian cycling of these parameter dependencies are

addressed in section 6.

5. Comparison of cycling sensitivity in different network structures. Our model analysis identifies differences in cycling mechanisms associated with the different structures of the proposed REM sleep regulatory networks, and it predicts the components of these networks that have the most significant effects on REM sleep dynamics. In this section, we summarize similarities and differences in the changes in dynamics due to modulation of the auto-effect and coupling parameters in the three networks.

The primary difference in network structures is the action of the synaptic input from R to N: this input is excitatory in the RI network and inhibitory in the MI networks. Interestingly, the effect of strengthening this input is distinguished in the dynamics of the models only by the response of the R population. Strengthening $g_{R,N}$ leads to suppression of the N population in all networks (panels C, D, and F in Figures 3, 6, and 8). However, in the RI network, suppression of N results in suppression of R, and model solutions approach steady states with both F_N and F_R at low values. By contrast, in the MI networks, suppression of N promotes R activation, and in the MIHN network, solutions approach steady states with F_N at low values and F_R at high values. In the MIHR network, strengthening $g_{R,N}$ disrupts cycling by introducing a stable threshold fixed point that occurs due to maintenance of R activation and N suppression (as described above). Thus, in both MI models, strengthening the input from R to N favors R activation and N suppression.

On the other hand, the coupling from N to R, governed by $g_{N,R}$, is inhibitory in all network structures, and this similarity in structure leads to similar changes in dynamics when model components related to this coupling are modulated. For example, increasing $g_{N,N}$ promotes N activation, thereby increasing values of F_N and amplifying the effect of $g_{N,R}$. In all model networks, strong self-excitation of the N population ($g_{N,N}$ large and positive) leads to persistent N activation and, thus, the persistent suppression of the R population (cyan regions in panels A, B, and C in Figures 3, 6, and 8). This structural similarity also underlies the common lack of cycling sensitivity to increases in $g_{N,R}$ in the RI and MIHN networks (panels B, D, and E in Figures 3 and 6). However, the MIHR model produces a distinct response to variation of this parameter: stable cycling solutions in the MIHR network are particularly sensitive to $g_{N,R}$ since sufficiently strong $g_{N,R}$ counteracts the homeostatic promotion of R activation and can introduce a system fixed point reflecting persistent R suppression and N activation (cyan regions in panels D and E of Figure 8).

Physiological constraints on self-effects of the R population ($g_{R,R}$) differ across the models. However, in all three networks, cycling is sensitive to self-inhibition of the R population. None of the models support cycling dynamics if the auto-effects of the R population are more than slightly inhibitory, and cycling in the RI model requires a minimum level of R self-excitation. Interestingly, although negative $g_{R,R}$ leads to steady suppression of the R population in all models, the resulting behavior of F_N differs: in the MIHR model, suppression of R allows activation of N (cyan region in panels A, E, and F in Figure 8); in the RI and MIHN models, suppression of R causes suppression of N (lavender regions in panels A, E, and F in Figures 3 and 6) through mechanisms involving loss of excitation and interaction with the homeostat, respectively.

Another dynamic similarity between the RI and MIHN networks is that strong self-

excitation of the R population leads to persistent activation of both the R and N populations (dark purple regions in panels A, E, and F in Figures 3 and 6). Additionally, in both models, loss of cycling due to high R self-excitation can be offset by increasing the strength of inhibition from N to R, $g_{N,R}$ (panel E in Figures 3 and 6). However, jointly varying $g_{R,R}$ and $g_{R,N}$, the strength of interaction from R to N, distinguishes the dynamics of these two models (panel F in Figures 3 and 6): loss of cycling in the RI model due to stronger $g_{R,N}$ can be restored by strengthening $g_{R,R}$, while cycling in the MIHN model requires weakening $g_{R,R}$. By contrast, strong self-excitation of the R population readily distinguishes the MIHR model by inducing persistent R activation but N suppression, which is robust to compensatory actions of any other parameter (panels A, E, and F in Figure 8).

In summary, analyzing dynamic responses to variations in different parameters among the models can both differentiate and identify commonalities among the cycling mechanisms acting within the network structures. The fundamental difference between the action of $g_{R,N}$ in the RI and MI networks causes differential responses to strengthening $g_{R,N}$ between the model networks. However, the RI and MIHN networks show similar dynamic responses to the variation of several different parameters, including $g_{R,R}$, $g_{N,N}$, $g_{N,R}$, and joint variation of $g_{R,R}$ and $g_{N,R}$. They show different responses, however, to the joint variation of $g_{R,R}$ and $g_{R,N}$. In the MIHR and MIHN networks, we observe common responses to variations in $g_{N,N}$ and strengthening of $g_{R,N}$; however, the differential site of action of the homeostat in these networks results in distinct dynamic responses to changes in $g_{R,R}$ and strengthening of $g_{N,R}$. In section 6, we will discuss the implications of these similarities and differences to the production of REM sleep in the whole animal and identify targets for experimental studies to probe the dynamic structure of the REM regulatory network.

6. Discussion. Motivated by the current debate on the neuronal mechanisms regulating REM sleep, we constructed minimal physiologically based mathematical models of the leading hypotheses for the structure of interactions between neuronal populations that regulate REM sleep transitions. The RI model reflects the classical RI hypothesis for REM sleep first proposed by McCarley and Hobson [32], and the MI models are based on recent studies identifying REM- and NREM-active populations coupled through GABAergic synaptic interactions [26, 4, 29, 42]. In the MI network structure, a REM sleep homeostatic drive plays a key role in transition dynamics. Although there is experimental evidence for such a drive, the physiological basis for the REM sleep homeostatic drive has not been determined. Therefore, we consider two models with an MI structure, MIHN and MIHR, in which a REM sleep homeostatic drive modulates activity in the REM-off (MIHN) or REM-on (MIHR) population. While these anatomical structures of synaptic interactions among the proposed REM sleep regulatory neuronal populations have been established experimentally in postmortem studies, the experimental investigation of their dynamic interactions, and thus the determination of the causal role any of these populations may play in REM sleep, is hampered by limitations in experimental technologies.

The transition dynamics among REM and NREM sleep states in the whole animal represent the primary experimentally accessible marker of the dynamics of the putative REM sleep regulatory network. Thus, for this modeling study, we concentrated on analyzing differences in dynamics among the three models that result from the differences in their underlying network

structure. We particularly focused on dynamics of regular cycling of alternating activity of the REM-on and REM-off populations which would generate the REM sleep ultradian cycle observed in human sleep. We determined necessary and sufficient conditions for the existence of stable limit cycle solutions in the RI model and stable hysteresis-loop cycling in the MIHN and MIHR models. Our analysis identified the sensitivity of cycling dynamics to changes in the key components of model networks: coupling parameters, representing efficacy of the synaptic projections between populations, and auto-effect parameters, reflecting intrinsic excitability properties of the populations. Our results show that although the networks display distinct dynamic responses to variations in specific coupling parameters, they can respond similarly to variations in others. Since network structure is the primary factor determining REM dynamics as coupling and auto-effect parameters are varied, the qualitative changes we report are robust to variation of other model parameters. Thus, our analysis may inform the interpretation of changes in REM sleep dynamics in a physiological network in response to specific experimental manipulations.

Stable periodic cycling solutions occur in the RI and MI networks by fundamentally different mechanisms requiring distinct necessary and sufficient conditions for their existence. Existence of the limit cycle solutions in the 2D RI model could be established by a straightforward determination of the absence of stable fixed points and the application of the Poincaré–Bendixson theorem. For the hysteresis-loop cycling solutions in the MI models, we exploited the inevitable slowness of the time scale of the REM sleep homeostatic drive (which is on the time scale of REM bout durations) relative to the fast time scales governing activity transitions of the REM-on and REM-off populations. The fast-slow decomposition of these 3D models allowed analysis of dynamics in terms of the bifurcation diagram and phase plane of the 2D fast subsystem. We developed the correlation between hysteresis-loop cycling in the fast subsystem bifurcation diagram and in the phase plane that then indicated how to construct the necessary and sufficient conditions for the existence of stable cycling.

6.1. Predictions for REM sleep regulation. The structures of the mathematical RI and MI model networks investigated herein were based on conceptual models suggested by extensive anatomical and physiological experimental work. The conceptual RI model, upon which our mathematical RI model is based, reflects the synaptic interactions between cholinergic REM-on subpopulations of laterodorsal tegmental nucleus (LDT) and pedunculopontine tegmental nucleus (PPT) with the noradrenergic locus coeruleus (LC) [25, 31]. This conceptual model posits that robust REM sleep cycling is caused by the dynamics of interaction between excitatory LDT/PPT neurons and inhibitory LC neurons. The conceptual MI model, upon which our mathematical MI models are based, has been linked to several candidate physiological networks. Lu and colleagues proposed that mutual GABAergic inhibition between the REM-on neurons in sublaterodorsal nucleus (SLD) and precoeruleus (PC) and REM-off neurons in the ventrolateral part of the periaqueductal gray matter (vlPAG) and lateral pontine tegmentum (LPT) represented the causal mechanism for REM sleep regulation [26]. McCarley and colleagues have suggested that mutual GABAergic inhibition between REM-on neurons in the subcoeruleus and pontine nucleus oralis (PnO) and REM-off neurons in the LPT forms a causal REM regulatory structure that is modulated by cholinergic inputs [4]. Luppi and colleagues have suggested a more complicated conceptual model in which largely

GABAergic interactions between REM-on neurons in posterior hypothalamus, vlPAG, SLD, dorsal paragigantocellular reticular nucleus (DPGi), and ventral gigantocellular reticular nucleus (GIV), and REM-off neurons in vlPAG and dorsal deep mesencephalic reticular nucleus (dDpMe) form a mutually inhibitory network structure [29, 42, 27, 28]. They further propose that vlPAG contains both REM-on and REM-off neurons so that local interactions within the vlPAG contribute to REM sleep regulation.

Given this physiological complexity, it is important to note that all of these neuronal populations co-exist in the brain and show appropriate state-dependent alterations in activity. However, it is not known which of these neuronal populations participates in a causal REM regulatory network, i.e., which populations play the primary causal role for REM sleep transitions and which display correlated (but not causal) state-dependent activity. The results of our model analysis suggest that the neuronal populations associated with the causal REM sleep network may be identified by evaluating distinct responses in REM sleep dynamics to experimental modulation of specific network components. Assuming one causal network, the modulation of neuronal populations in correlative networks should result in changes in their activity levels but should not significantly affect REM sleep dynamics. Experimental techniques allowing such experimental manipulations of these components in the intact animal may include targeted microinjection of neurotransmitter agonists/antagonists or other pharmacological agents; current injection protocols; or optogenetic techniques of targeted neuronal activation (reviewed in [2, 12]).

Experimental modulation of the dynamics of a neuronal population network requires a priori knowledge of the specific neurophysiology of the network. Therefore, the choice of specific synaptic pathways or neuronal populations targeted for manipulation contributes to the identification of the causal network for REM sleep regulation. In some cases, our analysis predicts that targeting analogous physiological components in different physiological networks will have similar effects on REM sleep regardless of the underlying network structure. For example, model analysis predicts that increasing activity of the associated REM-off population will suppress activity of the REM-on population, and thus suppress REM sleep, in both RI and MI network structures. On the other hand, our analysis clearly identifies cases in which network structure dictates different dynamic responses to manipulation of analogous network components. A primary target to distinguish a causal role for a physiological RI or MI network is the out-going synaptic pathway from the REM-on population, the key structural difference between the underlying conceptual models. Our model results predict that strengthening the efficacy of this pathway will disrupt REM sleep cycling, but the change in the activity of the REM-on population will distinguish the effects associated with different network structures. In the RI network, strengthening the REM-on to REM-off synaptic pathway will diminish activity in both the REM-on and REM-off populations and decrease REM sleep. In the MI network, strengthening the REM-on to REM-off synaptic pathway will enhance activity in the REM-on population and increase REM sleep. Thus, the type of change in REM sleep dynamics in response to this manipulation, as well as the synaptic pathway targeted by the manipulation, would predict the network structure associated with a causal role in REM sleep regulation.

Of equal importance, our model analysis identifies network components whose manipulation in a causal network may result in only negligible changes in REM sleep, and, thus, the

underlying causal role would not be identified. Specifically, strengthening the efficacy of the synaptic projection from the REM-off to the REM-on population may not significantly change REM sleep cycling in either a causal RI network or a causal MI network if transitions are governed as in the MIHN model. If transitions in the physiological MI network are governed as in the MIHR model, a causal role may be identified since model analysis predicts that REM sleep should decrease in response to strengthening this synaptic projection.

Within the structure of a causal MI network, our model analysis identifies several experimental manipulations that can distinguish the mechanisms generating transitions in activity, particularly whether transitions into REM sleep are caused by changes in activation of the REM-on or REM-off populations. If the REM sleep homeostatic drive acts on the REM-off population (corresponding to the MIHN model), the REM sleep state is initiated by the release of the REM-on population from decreasing inhibition from the REM-off population. If the REM sleep homeostat acts on the REM-on population (as in the MIHR model), REM sleep is initiated by increasing excitability of the REM-on population leading to its escape from inhibition from the REM-off population. Our model analysis highlights the distinction between the dynamics of release and escape from inhibition and predicts differing responses to modulation of specific network components related to these mechanisms. For example, the different predicted responses in the MI networks to strengthening the efficacy of the synaptic pathway from the REM-off to the REM-on population discussed above are directly related to differences in the dynamics of release and escape. REM sleep initiation by release of inhibition in this pathway is insensitive to its strength, while initiation through escape of inhibition will be suppressed as the efficacy of this pathway is strengthened. Thus, manipulating this pathway in a physiological MI network will distinguish these transition mechanisms. Another physiological target for manipulation that may distinguish transition mechanisms in the MI network is the activity of the REM-on population. Since the dynamics of release and escape from inhibition will yield similar changes to REM sleep in response to suppression or activation of this population, activity levels of the REM-on and REM-off populations must be tracked in order to distinguish these transition mechanisms. Suppression of the REM-on population will decrease REM sleep by suppressing activity in both the REM-on and REM-off populations if release of inhibition governs REM sleep initiation as in the MIHN model. However, in the case of the escape from inhibition mechanism as in the MIHR network, suppression of activity in the REM-on population will decrease REM sleep with promotion of activity in the REM-off population. Conversely, increasing activity in the REM-on population promotes REM sleep by promoting activity in the REM-on population when either release or escape mechanisms are governing REM initiation. The REM-off population will be jointly activated in the case of a release mechanism (MIHN model), while it will be suppressed with an escape mechanism (MIHR model). Thus, identifying the causal transition mechanisms in these scenarios would require monitoring firing rates of the REM-on and REM-off populations in addition to REM sleep dynamics.

In this study, we have concentrated on analyzing the existence of cycling behavior in the proposed REM sleep regulatory networks without placing constraints on the period of oscillatory solutions and thus the resulting durations of REM and NREM bouts. However, the sensitivity of the ultradian rhythm period to experimental manipulation of network components represents another source of constraints for the putative REM sleep regulatory networks,

as has been investigated in the original model implementation of the RI network structure [33]. Future work investigating the effects of external inputs and simulated experimental manipulation on the dynamics of these networks as well as embedding them within larger putative sleep-wake regulatory networks will allow for further distinctions among them.

6.2. Predictions for a REM sleep homeostatic drive. Evidence for the homeostatic regulation of REM sleep is provided by reported increases in REM sleep following either total sleep deprivation or REM selective sleep deprivation [1, 3, 21, 50, 5, 18]. A leading theory posits that the REM sleep homeostatic drive consists of two separate processes: a short-term process that controls NREM-REM sleep cycling and a long-term process that regulates the total daily amount of REM sleep [21]. The REM sleep homeostatic drive in our MI models would correspond to a short-term process. While experimental evidence suggests that forebrain mechanisms are involved in REM sleep homeostasis, the physiological substrates for the REM sleep homeostatic drive are unknown [10, 48, 23]. The difficulty in determining the physiological mechanisms responsible for REM sleep homeostasis stems from (1) the lack of identified markers for REM sleep need and REM sleep intensity whose variation could be monitored and correlated with disruptions to REM sleep, and (2) from the often subtle deprivation-induced changes in REM sleep that can be difficult to interpret due to competing compensatory changes in NREM sleep. Given this absence of hypothesized mechanisms, we based our implementation of the REM sleep homeostatic drive on our previously developed homeostatic drive for sleep motivated by the action of adenosine [14]. We further considered the two obvious candidates for the site of action of the REM sleep homeostatic drive, namely, modulation of activity of the REM-on or REM-off population. An additional undetermined characteristic of the REM sleep homeostatic drive is whether it promotes or limits REM sleep (i.e., whether it facilitates transitions into or out of REM sleep). In our MI network model, we showed that REM drives acting on a particular population with either of these mechanisms are mathematically equivalent. Hence, our results considered only REM-terminating drives. However, this equivalency is limited to the situation where the network is isolated from other external inputs; if the population under homeostatic control also receives inputs from outside the network, we expect that differential responses to those inputs could occur depending on whether the homeostat was REM-promoting or REM-terminating.

In the MI network, our model analysis suggests targets for further experimental investigation of the REM sleep homeostatic drive. REM sleep cycling activity occurred more robustly if the REM homeostatic drive modulated the activity of the REM-off population, and thus the REM-on population activated via release from inhibition. This action of the REM homeostatic drive is similar to the current hypothesis for the general sleep homeostatic drive wherein adenosine concentration depends on time in waking but acts by modulating activity of the sleep-promoting ventrolateral preoptic nucleus [7, 35, 22]. Thus, we propose that further investigation of characteristics and properties of the identified REM-off populations, such as cell types, activity patterns, and neuromodulator sensitivities, may yield insights into the homeostatic control of REM sleep.

The dynamics of our two MI model networks, MIHN and MIHR, were similar with equivalent conditions for the existence of cycling and mechanisms inducing the loss of cycling. However, the MIHR model showed one type of solution that does not occur in the MIHN

model, namely, high-amplitude cycling activity in the REM-on population with steady activity in the REM-off population. This solution was stable in a parameter regime where both the REM-on and REM-off populations were self-excitatory (Figure 8A, red region). While this cycling solution was not particularly robust to parameter variation, and thus is not expected to be a physiologically stable activity pattern, its existence raises the possibility that REM cycling may not be generated strictly by network interactions. In this solution, the hysteresis loop occurs due to the interaction of positive feedback in the REM-on population and the homeostatic control of its excitability. The REM-off population does not contribute to transitions in activity of the REM-on population since its strong self-excitation keeps it persistently activated. Thus, it may be possible that REM sleep cycling is autoregulated by the activity of a REM-on population under homeostatic control, and synaptic interactions with REM-off populations may modulate, but not cause, REM sleep transitions. Similarly, a REM sleep homeostatic drive could play a modulatory or stabilizing role in a network with an RI structure, even though such a network is capable of producing robust cyclic alternations between REM and NREM sleep in the absence of external drives. Future work examining these possibilities may provide additional insights into the role of the REM sleep homeostatic drive in the regulation of REM sleep.

6.3. Implications of modeling formalism. In these analyses, our choice of modeling formalism may represent a key constraint on system behavior, particularly for the MI networks. The equations we use to describe firing rate in each neuronal population do not support intrinsic properties of excitability or oscillations. Therefore, in the MI networks an external forcing function is necessary to achieve robust oscillations. In other models of sleep-wake regulation implementing different mathematical formalisms for neuronal population activity, cyclic alternation between mutually inhibitory REM-on and REM-off neuronal populations may occur without an external forcing function due to each population possessing intrinsic oscillatory dynamics or dynamics that support excitable responses following inhibitory input [38]. Our modeling formalism also differs from the numerous mutually inhibitory neuronal network models generating robust antiphase oscillatory behavior underlying central pattern generators in the nervous system of many species [49, 45]. Oscillations in these networks, often referred to as half-center oscillator networks, rely on properties of excitability and intrinsic oscillation inherent in models of neuronal action potential generation to support robust cycling behavior. In our MI network models, MIHN and MIHR, the critical role of the REM sleep homeostatic drive for generating transitions in REM-on and REM-off population activity levels results in particular sensitivities to the mathematical formulation of the homeostatic variable $h(t)$. One characteristic of its formulation is the potential for saturation of h at either a low or a high value, set to 0 and 1, respectively. For the general sleep homeostat based on the action of adenosine, the imposition of saturation limits on the homeostatic variable reflects the expected saturation of adenosine concentration, or the saturation of the action of adenosine receptors on neuronal activity. We assume an analogous chemical basis for the REM sleep homeostatic drive. As a result, we expect that the loss of cycling due to the introduction of a system fixed point as a result of saturation properties of h accurately reflects a mechanism that may occur in the physiological network.

Another characteristic of the mathematical formulation of the REM sleep homeostatic

drive is the definition of the threshold $F_R = \theta_R$ for REM-on activity which determines the direction of variation of h. Our choice of a single threshold value to mark both the activation and inactivation of F_R, and thus the occurrence and cessation, respectively, of REM sleep, was motivated by the goal of keeping the models as parsimonious as possible in the absence of physiologically indicated mechanisms. However, when REM sleep is determined entirely by the activity of a single population with respect to a single activation threshold, the potentially spurious model solutions we termed stable threshold fixed points are introduced. In these solutions, model trajectories are trapped as h alternates its direction of movement across this threshold. While cycling dynamics are lost when a stable threshold fixed point is introduced, the underlying mechanisms that can support cycling may not be destroyed. Hence, cycling can still be possible in these parameter regions if the mathematical formulation governing h is modified.

To understand this dependence on the formulation of h, we consider the mechanisms discussed in sections 4.1.2 and 4.2.2 describing the introduction of stable threshold fixed points in response to parameter variation. Stable threshold fixed point solutions occur when there is a stable conditional fixed point associated with $F_R = \theta_R$. One mechanism by which stable threshold fixed points are introduced is when the bifurcation curve of the fast subsystem has the proper Z-shape and bistability of stable steady states to support hysteresis-loop cycling, but one of the stable steady-state branches crosses $F_R = \theta_R$ within the interval $0 \leq h \leq 1$. This case occurs primarily in the MIHR model. In this case, cycling can be restored if the value of θ_R is changed so as to intersect only the unstable branch of the bifurcation curve. Another mechanism by which a stable threshold fixed point is introduced is when the bifurcation curve of the fast subsystem is distorted so that the bistability region of stable steady states is lost, and all steady-state solutions on the curve are stable, including the steady state at $F_R = \theta_R$. In this case, cycling can be restored by implementing a more complicated thresholding mechanism for h activity, such as separate thresholds for the activation and inactivation of F_R. Given the dependence of cycling on the mathematical formulation of h in these cases, we do not interpret the introduction of a stable threshold fixed point as a robust mechanism that can destroy cycling in the physiological network. Instead, we identify this mechanism as a possible consequence of a REM sleep homeostatic drive that may affect dynamics in the physiological network.

6.4. Relating results to prior sleep-wake regulatory network models. The network structures of our RI and MI models are present in other mathematical models of the sleep-wake regulatory network. We noted above that differences in mathematical formalism may lead to different relationships between structure and dynamics despite similarities in network structure. However, in many cases, similarities between structure and dynamics across models may be observed. In the 1970s, McCarley and Hobson introduced an RI model for REM sleep regulation [32]. In their mathematical model, REM-on and REM-off neuronal populations were coupled together through inhibitory and excitatory coupling, respectively. The population interaction was described using modified Lotka–Volterra equations in which the strength of interactions is proportional to the product of population activities, similar to mass action coupling in chemical kinetic models and species interactions that depend on population size. In subsequent work, the original model was refined so that oscillations between NREM and

REM sleep were stable limit cycle solutions, but the coupling formalism remained the same [33]. Our modeling formalism is based on neuronal population firing rate models, developed in the field of computational neuroscience [51, 11, 9, 19, 14]. However, our RI model also robustly displays stable limit cycle solutions generated by the excitatory and inhibitory coupling between populations.

The hysteresis-loop cycling between REM and NREM sleep states that occurs in our MIHN model is similar to the mechanism governing transitions between sleep and wake states in an MI network model for sleep-wake regulation proposed by Phillips and Robinson [36]. They employ a modestly different neuronal population firing rate model formalism to form a mutually inhibitory network that is driven to generate alternating activity in wake- and sleep-promoting populations by state-dependent external inputs. Since their model structure does not include self-effects, they can compute explicitly the parameter regions associated with hysteresis-loop cycling. Our results extend this approach by including models in which self-effects and different actions of the (REM sleep) homeostatic drive affect cycling. Our results also explain how specific characteristics of the REM homeostat, such as saturation and thresholding mechanisms, can critically affect stable cycling solutions (see section 6.3).

Many recent models of sleep-wake regulation have focused on the interaction among the three states of wake, NREM sleep, and REM sleep [17, 14, 16, 15, 38, 47]. Although we do not address the dynamics of wake and sleep transitions in this work, the RI and MI networks may be viewed as substructures within larger networks regulating these three states. As such, activity in other components of the larger network may act as external drives to the REM-regulating subnetwork. The influence of such external inputs to the RI and MI networks will allow for further distinctions in the dynamics of our different models. In particular, distinctions between REM-promoting and REM-terminating actions of the REM sleep homeostatic drive become significant in the presence of external inputs to either the REM-on or the REM-off populations. External inputs to the REM-regulating subnetwork may also facilitate the incorporation of additional features of REM sleep dynamics into the model. For example, the increasing duty cycle of REM sleep over the course of the human sleep period may represent a specific modulation of the REM-regulatory network by an external drive associated with circadian signaling by the SCN. Future work constructing three-state network models based on the distinct hypotheses for REM sleep regulation will provide more insight into the behavioral state transition dynamics predicted by different underlying network structures.

REFERENCES

[1] D. Aeschbach, *REM-sleep regulation: Circadian, homeostatic, and non-REM sleep-dependent determinants*, in Rapid Eye Movement Sleep: Regulation and Function, B. Mallick, S. Pandi-Perumal, R. McCarley, and A. Morrison, eds., Cambridge University Press, Cambridge, UK, 2011.

[2] H. A. Baghdoyan and R. Lydic, *Neurotransmitters and neuromodulators regulating sleep*, in Sleep and Epilepsy: The Clinical Spectrum, C. Bazil, B. Malow, and M. Sammaritano, eds., Elsevier Science, New York, 2002, pp. 17–44.

[3] J. Benington and H. Heller, *REM-sleep timing is controlled homeostatically by accumulation of REM-sleep propensity in non-REM sleep*, Amer. J. Physiol., 266 (1994), pp. 1992–2000.

[4] R. Brown, J. McKenna, S. Winston, R. Basheer, Y. Yanagawa, M. Thakkar, and R. McCarley, *Characterization of GABAergic neurons in rapid-eye-movement sleep controlling regions of the brainstem reticular formation in GAD67-green fluorescent protein knock-in mice*, Eur. J. Neurosci., 27 (2008), pp. 352–363.
[5] D. Brunner, D.-J. Dijk, I. Tobler, and A. Borbély, *Effect of partial sleep deprivation on sleep stages and EEG power spectra: Evidence for non-REM and REM sleep homeostasis*, EEG and Clin. Neurophysiol., 75 (1990), pp. 492–499.
[6] M. Carskadon and W. Dement, *Normal human sleep: An overview*, in Principles and Practice of Sleep Medicine, M. Kryger, T. Roth, and W. Dement, eds., Elsevier Saunders, New York, 2011.
[7] N. L. Chamberlin, E. Arrigoni, T. C. Chou, T. E. Scammell, R. W. Greene, and C. B. Saper, *Effects of adenosine on GABAergic synaptic inputs to identified ventrolateral preoptic neurons*, Neuroscience, 119 (2003), pp. 913–918.
[8] S. Datta and R. R. Maclean, *Neurobiological mechanisms for the regulation of mammalian sleep-wake behavior: Reinterpretation of historical evidence and inclusion of contemporary cellular and molecular evidence*, Neurosci. Biobehav. Rev., 31 (2007), pp. 775–824.
[9] P. Dayan and L. Abbott, *Theoretical Neuroscience: Computational and Mathematical Modeling of Neural Systems*, MIT Press, Cambridge, MA, 2001.
[10] I. de Andres, M. Garson, and J. Villablanca, *The disconnected brain stem does not support rapid eye movement sleep rebound following selective deprivation*, SLEEP, 26 (2003), pp. 419–425.
[11] G. Deco, V. K. Jirsa, P. A. Robinson, M. Breakspear, and K. Friston, *The dynamic brain: From spiking neurons to neural masses and cortical fields*, PLoS Comput. Biol., 4 (2008), e1000092.
[12] K. Deisseroth, *Optogenetics*, Nature Methods, 8 (2011), pp. 26–29.
[13] D.-J. Dijk and C. Czeisler, *Contribution of the circadian pacemaker and the sleep homeostat to sleep propensity, sleep structure, electroencephalographic slow waves, and sleep spindle activity in humans*, J. Neurosci., 15 (1995), pp. 3526–3538.
[14] C. Diniz Behn and V. Booth, *Simulating microinjection experiments in a novel model of the rat sleep-wake regulatory network*, J. Neurophysiol., 103 (2010), pp. 1937–1953.
[15] C. Diniz Behn and V. Booth, *Modeling the temporal architecture of rat sleep-wake behavior*, in Proceedings of the IEEE Conference on Engineering in Medicine and Biological Science, IEEE, Washington, DC, 2011, pp. 4713–4716.
[16] C. G. Diniz Behn and V. Booth, *A fast-slow analysis of the dynamics of REM sleep*, SIAM J. Appl. Dyn. Syst., 11 (2012), pp. 212–242.
[17] C. G. Diniz Behn, E. N. Brown, T. E. Scammell, and N. J. Kopell, *A mathematical model of network dynamics governing mouse sleep-wake behavior*, J. Neurophysiol., 97 (2007), pp. 3828–3840.
[18] T. Endo, C. Roth, H.-P. Landolt, E. Werth, D. Aeschbach, P. Achermann, and A. Borbély, *Selection REM sleep deprivation in humans: Effects on sleep and sleep EEG*, AJP Regu. Physiol., 274 (1998), pp. R1186–R1194.
[19] G. Ermentrout, *Neural networks as spatio-temporal pattern-forming systems*, Rep. Progr. Phys., 61 (1998), pp. 353–430.
[20] M. Fleshner, V. Booth, D. B. Forger, and C. Diniz Behn, *Multiple signals from the suprachiasmatic nucleus required for circadian regulation of sleep-wake behavior in the nocturnal rat*, Phil. Trans. Roy. Soc. A, 369 (2011), pp. 3855–3883.
[21] P. Franken, *Long-term vs. short-term processes regulating REM sleep*, J. Sleep Res., 11 (2002), pp. 17–28.
[22] T. Gallopin, P. H. Luppi, B. Cauli, Y. Urade, J. Rossier, O. Hayaishi, B. Lambolez, and P. Fort, *The endogenous somnogen adenosine excites a subset of sleep-promoting neurons via A2A receptors in the ventrolateral preoptic nucleus*, Neuroscience, 134 (2005), pp. 1377–1390.
[23] I. Gvilia, A. Turner, D. McGinty, and R. Szymusiak, *Preoptic area neurons and the homeostatic regulation of rapid eye movement sleep*, J. Neurosci., 26 (2006), pp. 3037–3044.
[24] M. Hirsch, S. Smale, and R. Devaney, *Differential Equations, Dynamical Systems, and an Introduction to Chaos*, Academic Press, New York, 2004.
[25] J. Hobson, R. McCarley, and P. Wyzinski, *Sleep cycle oscillation: Reciprocal discharge by two brainstem neuronal groups*, Science, 189 (1975), pp. 55–58.

[26] J. Lu, D. Sherman, M. Devor, and C. B. Saper, *A putative flip-flop switch for control of REM sleep*, Nature, 441 (2006), pp. 589–594.
[27] P.-H. Luppi, O. Clement, E. Sapin, D. Gervasoni, C. Peyron, L. Leger, D. Salvert, and P. Fort, *The neuronal network responsible for paradoxical sleep and its dysfunctions causing narcolepsy and rapid eye movement (REM) behavior disorder*, Sleep Med. Rev., 15 (2011), pp. 153–163.
[28] P. H. Luppi, O. Clement, E. Sapin, C. Peyron, D. Gervasoni, L. Leger, and P. Fort, *Brainstem mechanisms of paradoxical (REM) sleep generation*, Pflugers Arch., 463 (2012), pp. 43–52.
[29] P. H. Luppi, D. Gervasoni, L. Verret, R. Goutagny, C. Peyron, D. Salvert, L. Leger, and P. Fort, *Paradoxical (REM) sleep genesis: The switch from an aminergic-cholinergic to a GABAergic-glutamatergic hypothesis*, J. Physiol. Paris, 100 (2006), pp. 271–283.
[30] S. G. Massaquoi and R. W. McCarley, *Extension of the limit cycle reciprocal interaction model of REM cycle control. An integrated sleep control model*, J. Sleep Res., 1 (1992), pp. 138–143.
[31] R. W. McCarley, *Mechanisms and models of REM sleep control*, Arch. Ital. Biol., 142 (2004), pp. 429–467.
[32] R. W. McCarley and J. A. Hobson, *Neuronal excitability modulation over the sleep cycle: A structural and mathematical model*, Science, 189 (1975), pp. 58–60.
[33] R. W. McCarley and S. G. Massaquoi, *A limit cycle mathematical model of the REM sleep oscillator system*, Am. J. Physiol., 251 (1986), pp. R1011–R1029.
[34] D. McGinty and R. Szymusiak, *Neural control of sleep in mammals*, in Principles and Practice of Sleep Medicine, M. Kryger, T. Roth, and W. Dement, eds., Elsevier Saunders, New York, 2011, pp. 76–91.
[35] S. Morairty, D. Rainnie, R. McCarley, and R. Greene, *Disinhibition of ventrolateral preoptic area sleep-active neurons by adenosine: A new mechanism for sleep promotion*, Neuroscience, 123 (2004), pp. 451–457.
[36] A. J. Phillips and P. A. Robinson, *A quantitative model of sleep-wake dynamics based on the physiology of the brainstem ascending arousal system*, J. Biol. Rhythms, 22 (2007), pp. 167–179.
[37] T. Porkka-Heiskanen, R. E. Strecker, and R. W. McCarley, *Brain site-specificity of extracellular adenosine concentration changes during sleep deprivation and spontaneous sleep: An in vivo microdialysis study*, Neuroscience, 99 (2000), pp. 507–517.
[38] M. J. Rempe, J. Best, and D. Terman, *A mathematical model of the sleep/wake cycle*, J. Math. Biol., 60 (2010), pp. 615–644.
[39] J. Rinzel, *Bursting oscillations in an excitable membrane model*, in Ordinary and Partial Differential Equations: Proceedings of the 8th Dundee Conference, B. Sleeman and R. Jarvis, eds., Lecture Notes Math. 1151, Springer, New York, 1985, pp. 304–316.
[40] C. B. Saper, T. C. Chou, and T. E. Scammell, *The sleep switch: Hypothalamic control of sleep and wakefulness*, Trends Neurosci., 24 (2001), pp. 726–731.
[41] C. B. Saper, T. E. Scammell, and J. Lu, *Hypothalamic regulation of sleep and circadian rhythms*, Nature, 437 (2005), pp. 1257–1263.
[42] E. Sapin, D. Lapray, A. Berod, R. Goutagny, L. Leger, P. Ravassard, O. Clement, L. Hanriot, P. Fort, and P. H. Luppi, *Localization of the brainstem GABAergic neurons controlling paradoxical (REM) sleep*, PLoS One, 4 (2009), e4272.
[43] T. E. Scammell, D. Y. Gerashchenko, T. Mochizuki, M. T. McCarthy, I. V. Estabrooke, C. A. Sears, C. B. Saper, Y. Urade, and O. Hayaishi, *An adenosine A2a agonist increases sleep and induces Fos in ventrolateral preoptic neurons*, Neuroscience, 107 (2001), pp. 653–663.
[44] J. M. Siegel, *REM sleep*, in Principles and Practice of Sleep Medicine, M. Kryger, T. Roth, and W. Dement, eds., Elsevier Saunders, New York, 2011, pp. 92–111.
[45] F. Skinner, N. Kopell, and E. Marder, *Mechanisms for oscillation and frequency control in networks of mutually inhibitory relaxation oscillators*, J. Comput. Neurosci., 1 (1994), pp. 69–87.
[46] R. E. Strecker, S. Morairty, M. M. Thakkar, T. Porkka-Heiskanen, R. Basheer, L. J. Dauphin, D. G. Rainnie, C. M. Portas, R. W. Greene, and R. W. McCarley, *Adenosinergic modulation of basal forebrain and preoptic/anterior hypothalamic neuronal activity in the control of behavioral state*, Behav. Brain Res., 115 (2000), pp. 183–204.
[47] Y. Tamakawa, A. Karashima, Y. Koyama, N. Katayama, and M. Nakao, *A quartet neural system model orchestrating sleep and wakefulness mechanisms*, J. Neurophysiol., 95 (2006), pp. 2055–2069.

[48] L. Verret, R. Goutagny, P. Fort, L. Cagnon, D. Salvert, L. Leger, R. Boissard, P. Salin, C. Peyron, and P.-H. Luppi, *A role of melanin-concentrating hormone producing neurons in the central regulation of paradoxical sleep*, BMC Neurosci., 4 (2003), p. 19.

[49] X.-J. Wang and J. Rinzel, *Alternating and synchronous rhythms in reciprocally inhibitory model neurons*, Neural Comput., 4 (1992), pp. 84–97.

[50] E. Werth, K. Cote, E. Gallmann, A. Borbély, and P. Achermann, *Time course of interventions and recovery sleep*, AJP Regu. Physiol., 283 (2002), pp. R521–R526.

[51] H. R. Wilson and J. D. Cowan, *Excitatory and inhibitory interactions in localized populations of model neurons*, Biophys. J., 12 (1972), pp. 1–24.